2012-09

The Aerodynamics of a Maneuvering UCAV 1303 Aircraft Model and its Control through Leading Edge Curvature Change

Medford, Christopher M.

Monterey, California. Naval Postgraduate School

NAVAL POSTGRADUATE SCHOOL

MONTEREY, CALIFORNIA

THESIS

THE AERODYNAMICS OF A MANEUVERING UCAV 1303 AIRCRAFT MODEL AND ITS CONTROL THROUGH LEADING EDGE CURVATURE CHANGE

by

Christopher M. Medford

September 2012

Thesis Advisor:	M. S. Chandrasekhara
Second Reader:	G. V. Hobson

Approved for public release; distribution is unlimited

THIS PAGE INTENTIONALLY LEFT BLANK

REPORT DOCUMENTATION PAGE			Form Approved OMB No. 0704–0188

1. AGENCY USE ONLY *(Leave blank)*	**2. REPORT DATE** September 2012	**3. REPORT TYPE AND DATES COVERED** Master's Thesis

4. TITLE AND SUBTITLE The Aerodynamics of a Maneuvering UCAV 1303 Aircraft Model and its Control through Leading Edge Curvature Change

5. FUNDING NUMBERS

6. AUTHOR(S) Christopher M. Medford

7. PERFORMING ORGANIZATION NAME(S) AND ADDRESS(ES)
Naval Postgraduate School
Monterey, CA 93943–5000

8. PERFORMING ORGANIZATION REPORT NUMBER

9. SPONSORING /MONITORING AGENCY NAME(S) AND ADDRESS(ES)
N/A

10. SPONSORING/MONITORING AGENCY REPORT NUMBER

11. SUPPLEMENTARY NOTES The views expressed in this thesis are those of the author and do not reflect the official policy or position of the Department of Defense or the U.S. Government. IRB Protocol number _____N/A_____.

12a. DISTRIBUTION / AVAILABILITY STATEMENT
Approved for public release; distribution is unlimited

12b. DISTRIBUTION CODE

13. ABSTRACT (maximum 200 words)

This study investigates the aerodynamic effects of modifying the leading edge on an unmanned combat air vehicle (UCAV) 1303. Literature suggests that leading edge accelerations are reduced for rounder leading edges and stall characteristics are altered. These phenomena are examined using the previously tested 1/72 scale model with a 47-degree leading edge sweep and a cranked trailing edge delta wing with fuselage.

The study consists of both flow visualization and aerodynamic force and moment measurements. The model is maneuvered in the NPS water tunnel where a five-component strain gage load balance system measures the forces experienced by it. The model is pitched at different rates with different degrees of yaw for these studies. This process is repeated for a modified leading edge with a radius double the baseline.

Preliminary results show that the rounded leading edge acted as expected, alleviating signs of tip-stall in the normal force distribution and smoothing pitch-breaks in the pitching moment distribution. Rolling moment was shown to increase with angle of attack for the modified leading edge case.

14. SUBJECT TERMS
Unmanned Combat Air Vehicle, UCAV, UCAV 1303, Tip Stall, Leading Edge

15. NUMBER OF PAGES 83

16. PRICE CODE

17. SECURITY CLASSIFICATION OF REPORT	**18. SECURITY CLASSIFICATION OF THIS PAGE**	**19. SECURITY CLASSIFICATION OF ABSTRACT**	**20. LIMITATION OF ABSTRACT**
Unclassified	Unclassified	Unclassified	UU

NSN 7540–01–280–5500 Standard Form 298 (Rev. 2–89)
Prescribed by ANSI Std. 239–18

THIS PAGE INTENTIONALLY LEFT BLANK

Approved for public release; distribution is unlimited

THE AERODYNAMICS OF A MANEUVERING UCAV 1303 AIRCRAFT MODEL AND ITS CONTROL THROUGH LEADING EDGE CURVATURE CHANGE

Christopher M. Medford
Ensign, United States Navy
B.S., United States Naval Academy, 2011

Submitted in partial fulfillment of the
requirements for the degree of

MASTER OF SCIENCE IN MECHANICAL ENGINEERING

from the

NAVAL POSTGRADUATE SCHOOL
September 2012

Author: Christopher M. Medford

Approved by: M. S. Chandrasekhara
Thesis Advisor

G. V. Hobson
Second Reader

K. T. Millsaps
Chair, Department of Mechanical and Aerospace Engineering

THIS PAGE INTENTIONALLY LEFT BLANK

ABSTRACT

This study investigates the aerodynamic effects of modifying the leading edge on an unmanned combat air vehicle (UCAV) 1303. Literature suggests that leading edge accelerations are reduced for rounder leading edges and stall characteristics are altered. These phenomena are examined using the previously tested 1/72 scale model with a 47-degree leading edge sweep and a cranked trailing edge delta wing with fuselage.

The study consists of both flow visualization and aerodynamic force and moment measurements. The model is maneuvered in the NPS water tunnel where a five-component strain gage load balance system measures the forces experienced by it. The model is pitched at different rates with different degrees of yaw for these studies. This process is repeated for a modified leading edge with a radius double the baseline.

Preliminary results show that the rounded leading edge acted as expected, alleviating signs of tip-stall in the normal force distribution and smoothing pitch-breaks in the pitching moment distribution. Rolling moment was shown to increase with angle of attack for the modified leading edge case.

THIS PAGE INTENTIONALLY LEFT BLANK

TABLE OF CONTENTS

THIS PAGE INTENTIONALLY LEFT BLANK

LIST OF FIGURES

LIST OF TABLES

THIS PAGE INTENTIONALLY LEFT BLANK

LIST OF ACRONYMS AND ABBREVIATIONS

AoA = Angle of Attack (deg.)

A_p = Planform area (m^2)

b = Wing Span (m)

c = Root Chord (m)

$\bar{c}$ = Mean Aerodynamic Chord (m)

C_L = Lift Coefficient ($\frac{L}{0.5\rho U_\infty^2 A_p}$)

C_M = Pitching Moment Coefficient ($\frac{PM}{0.5\rho U_\infty^2 A_p \bar{c}}$)

C_N = Normal Force Coefficient ($\frac{N}{0.5\rho U_\infty^2 A_p}$)

C_{RM} = Rolling Moment Coefficient ($\frac{RM}{0.5\rho U_\infty^2 A_p b}$)

C_S = Side Force Coefficient ($\frac{S}{0.5\rho U_\infty^2 A_p}$)

C_{YM} = Yawing Moment Coefficient ($\frac{YM}{0.5\rho U_\infty^2 A_p b}$)

L = Lift Force (N)

LEV = Leading Edge Vortex

M = Mach Number

N = Normal Force (N)

PM = Pitching Moment (N·m)

q = Dynamic Pressure (Pa)

Re = Reynolds Number

RM = Rolling Moment (N·m)

S = Side Force (N)

s = Semi-span (m)

U_∞ = Free-stream Velocity (m/s)

UCAV= Unmanned Combat Air Vehicle

YM = Yawing Moment (N·m)

α = Angle Alpha; AoA (deg.)

α+ = Non-dimensional Pitch Rate

$\dot{\alpha}$ = Pitch Rate (deg./s)

β = Sideslip Angle (deg.)

$\dot{\beta}$ = Yawing Rate (deg./s)

ρ = Fluid Density (kg/m^3)

ACKNOWLEDGMENTS

I would like to first and foremost thank Professor M. S. Chandrasekhara. He has encouraged me to always achieve greater understanding of problems I never thought I could comprehend. He has taught me many lessons in the research field and somehow remained patient with me through every one. He has expertise and insight—both in and out of aerodynamics—as well as an ability to communicate his knowledge. This has been a tremendous help throughout the process of this work. I would not have been able to accomplish any of this without his support throughout the previous year.

I also received several hours of patient attention from Mr. Mike Kerho and Mr. Brian Kramer of Rolling Hills Research Corporation, as well as from Mr. John Mobley of the NPS machine shop. Without their help, I would have never been able to operate the water tunnel, and the work was easier knowing their expertise was never far away.

Partial assistance was also received from the Singapore TDSI/Temasek Group under grant number TDSI/07–005/1A.

Finally, I would like to express my appreciation for my wife, Stephanie. She has been supportive and understanding of every effort needed to complete this thesis, and her love is inspirational to everyone she meets. I cannot love and thank you enough for your support throughout this journey.

THIS PAGE INTENTIONALLY LEFT BLANK

I. INTRODUCTION

A. OVERVIEW

Aeronauts have expressed interest in aerial warfare for hundreds of years. This idea has progressed from the use of balloons for surveillance, communication, and cartography to the leveling of cities from several thousand feet. Perhaps the latest and most viable concept today is the unmanned combat air vehicle (UCAV) or combat drone: a revolutionary addition to the current arsenal of airpower that has many unique advantages and therefore missions. The primary advantage of the UCAV is that it does not require an onboard pilot, removing the risk of losing personnel, especially in enemy territory. It also means that all of the human safety and interface devices, such as the cockpit, flight controls, oxygen systems, and ejection seat, can be removed. This leaves a smaller, lighter, and more maneuverable airframe which can be designed for performance and stealth since human factors no longer need to be considered. There is also a demand that the next generation of unmanned flight be unrestricted in maneuvers so that UCAVs can reliably participate in national defense missions such as Intelligence, Surveillance, and Reconnaissance (ISR), strike, and Suppression of Enemy Air Defenses (SEAD). Reliable participation means that the UCAV can evade oncoming threats and also perform desirably in the presence of strong crosswinds, gusts, and other uncontrollable perturbations. The UCAV should be aircraft carrier compatible, and no target is considered out of reach. This creates an elaborate flight envelope which encompasses very high angles of attack. This advanced maneuverability and do-it-all capability comes at a price, however.

Unmanned aircraft are often designed to operate in a stealthy mode, which results in fewer and smaller control surfaces. As a result, the aircraft generally flies at the fringes of aerodynamic stability [1]. Quite often, undesirable flow patterns develop over the aerodynamic surfaces. This is particularly true during maneuvers since the flow is unsteady, and the vehicle is rapidly thrust into different orientations. If these flow conditions setup over the control surfaces, and the UCAV cannot be recovered due to

lack of control authority, the cost could be tremendous because the secrets and technology carried on board could be compromised along with the security of the operators and the nation. It is therefore imperative to obtain a full understanding of the many possible unsteady flow conditions and to develop airfoil geometry that performs satisfactorily under such adverse flight conditions.

Contracted by the Air Force, Boeing Co. developed the UCAV 1303 design by modifying its original 1301 configuration [2]. Its flying wing shape, with low observables and no vertical tails, reflects the potential stealthy nature of its missions. This low profile aircraft lacks the extra control and aerodynamic surfaces found on many other flying vehicles. Tests have shown that it is inherently unstable in both the static and dynamic regimes [1]. It is currently an edge-aligned, near-lambda delta wing featuring two trailing edge cranks: a concave trailing edge crank near the mid-semi-span and an outboard convex trailing edge crank closer to the pointed wing tip. Boeing decreased the 1301's 50° leading edge sweep to a broader 47°, and increased the trailing edge angle from 20° to 30°. These modifications increased the aspect ratio from 3.07 to 3.85 [2]. The aft-rounded tips and blending wing-body configuration is representative of various UCAV models. The Boeing UCAV 1303 is shown in Figure 1.

Figure 1. Boeing UCAV 1303. From [3].

B. FLOW ASPECTS

As a nonslender wing, the UCAV 1303 behaves differently than the classically studied slender-bodied delta wing. At angles of attack beginning around 10 degrees, a slender wing's aerodynamic flow pattern is dominated by two large counter-rotating vortices generated along the entire leading edge as well as the control surfaces. These vortices form at higher angles of attack as a result of the flow shear layers' inability to overcome the adverse pressure gradient around the leading edge. This causes the flow to separate from the wing body and roll up [4]. Two energetic vortices are produced, in which the axial velocities can be as high as twice the freestream velocity [5]. The low local surface pressures associated with the high velocities in the vortex cores create a pressure differential between the top and bottom of the wing producing extra lift, called vortex lift. It is also common for secondary and tertiary vortices to form as local boundary layers separate through interactions with the main vortex.

Rapid motion, such as that of a maneuver, can result in flow separation delay, and results in vortex formation to occur at higher angles of attack, and vortex location also changes. Eventually, at some critical angle, all vortices breakdown. In one type of break down, flow stagnates in the core, and the core size expands by a factor of about three [4]. As a result, intense pressure fluctuations develop during the vortex breakdown phase. This rapidly changes the longitudinal and lateral loading of the aircraft, and a rapid loss in lift is experienced along with adverse pitching moment fluctuations. It is therefore desirable to delay vortex bursting as long as possible since its formation cannot be prevented easily. Figure 2 shows leading edge vortices forming and breaking down over a slender-bodied delta wing.

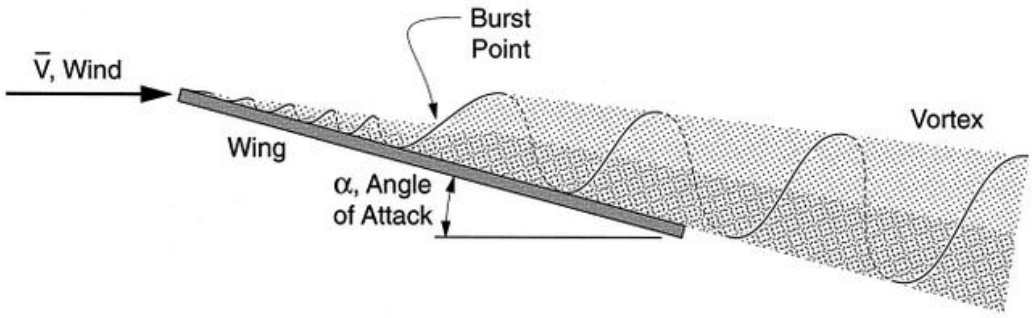

Figure 2. Representation of Vortex Bursting over a Delta Wing. From [6].

The flow over a UCAV 1303 model is known to produce weaker vortices [7] which results in a much smaller lift increase unlike the dramatic lift enhancements observed over slender wings at high angles of attack. Nonslender wing vortices form closer to the surface leading to a strong interaction between the vortex and the local boundary layer [7]. In this case, a dual primary vortex structure has been demonstrated to form both in computational and experimental studies [8]. In comparison to the strong leading edge vortices of the slender delta wing, very little is known about this near surface dual primary vortex structure. This structure is neither well defined nor exceptionally strong. It develops at considerably lower angles of attack and tends to break down at similarly lower angles compared to that over the slender wing. The dual vortex does contribute to extra lift, however—as well as its loss when it breaks down. Another consequence of the viscous/inviscid interaction is increased sensitivity to Reynolds number that is not experienced by slender wings [7].

1. Dominant Flow Events

Steady flow field over the UCAV 1303 have been previously studied, most notably in an effort to validate the CFD models that have been created [9], [10], [11]. One significant result is the appearance of a pitch-break in pitching moment at certain angles of attack. One cause for the pitch-break is tip-stall, which has been shown in flow visualization studies performed at the Naval Postgraduate School [3], [12]. Figure 3 demonstrates the occurrence of tip-stall at very low angles of attack from the vortical flow developing near the trailing edge crank in the wake. As the vortex bursts (see white

arrows), the flow spreads over the wings and propagates upstream, inducing tip-stall. Ol [13] has also noticed tip-stall in his experiments and attributed this to the sharp end at the end of the wingspan. He also validated the lack of a primary vortex structure as discussed previously. Figure 3, however, presents a more comprehensive description of the related events.

Figure 3. Close up of Tip-Stall from Trailing Edge Crank Vortex Bursting in Wake. Re = 4100, α = 6 degrees, steady flow. From [1].

A consequence of tip-stall is a break in both the normal force and pitching moment at the appropriate angle of attack in their distributions. The effect of tip-stall at α = 4° can be seen in both the pitching moment and normal force coefficients in Figure 4. The flow recovers from tip-stall with increasing angle of attack, since at a slightly higher angle, vortical flow also develops. The events of vortex formation and breakdown are also indicated in these plots.

The UCAV 1303 flow also develops a vortex system over its wings, although this is different from that seen for slender delta wings. The well-known leading vortex forms, but not as a whole structure from the leading edge boundary layer roll-up like that seen in case of the slender delta wing, but from the trailing edge of this same flow. Depending upon whether there is a fuselage present or not, the flow from the apex of the model also forms a vortex. Thus, two vortices of the same sign co-exist on the wing, as described in [1]. These vortices, however, seem to be weaker than the slender delta wing vortex, and are therefore responsible for a more gradual normal force variation. This variation is also quantified in a smaller value. Eventually, these vortices breakdown: each through a different mechanism [1].

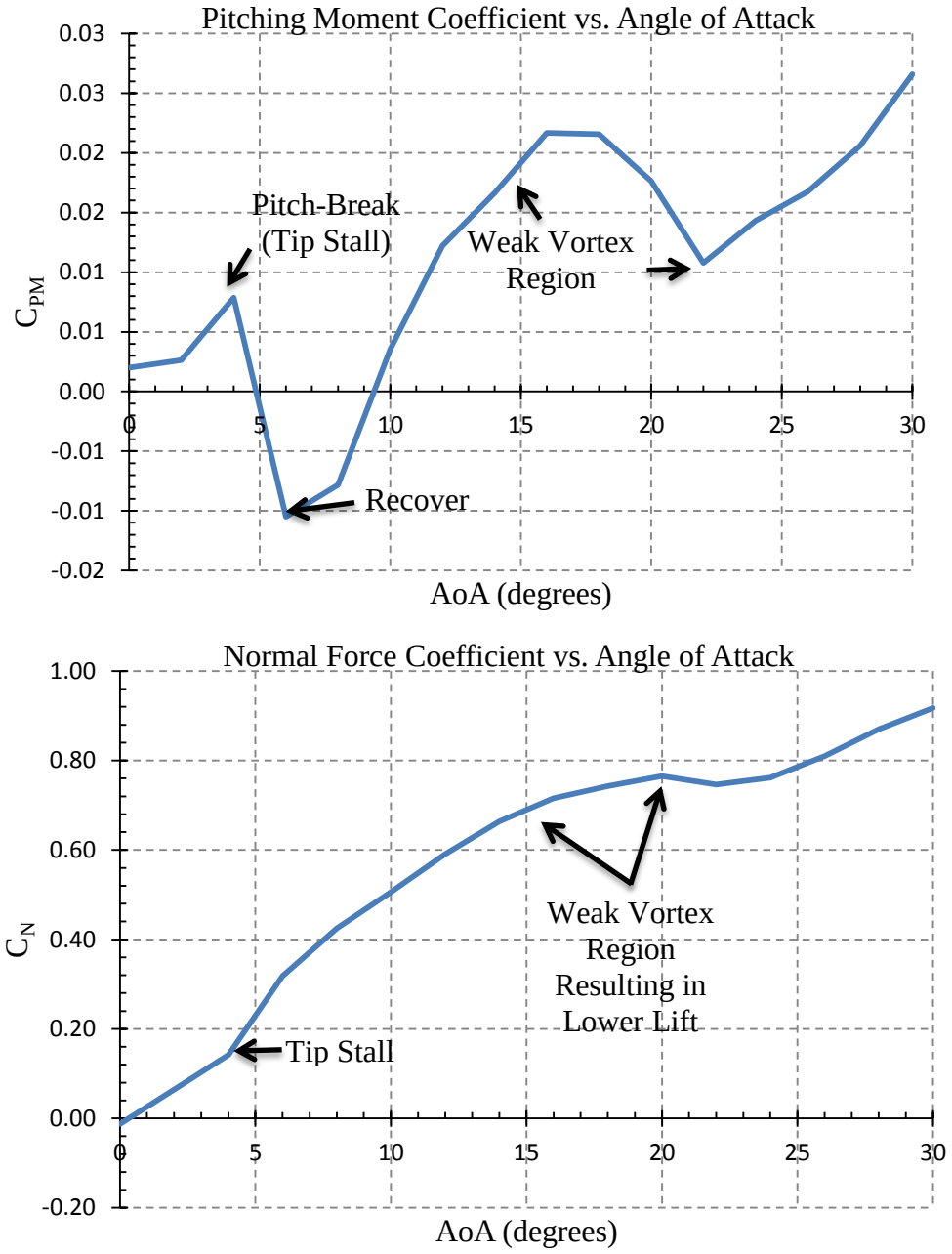

Figure 4. Variation and "Breaks" of Pitching Moment and Normal Force Coefficients, Re = 2.3 x 10^4, steady flow.

2. Pitch-Up Maneuver

There is limited literature or data collection of the flow field around a maneuvering UCAV 1303. The most thorough research has been by McLain [3] and

Sosebee [12]. Prior to these, Cummings et al. studied a pitching UCAV 1301 and verified the occurrence of pitch-break and dynamic stall [14]. Dynamic stall occurs on a rapidly pitching aerodynamic surface. Such unsteady maneuvers could generate additional lift, but only for the duration of the maneuver and should be considered when establishing the flight envelope for the aircraft. The extra lift, especially at high angles of attack, could be extremely useful at critical times of flight such as while evading a potential threat.

The pitch rates in the present experiments have been nondimensionalized for comparison as $\alpha+ = \frac{\dot{\alpha}\bar{c}}{U_\infty}$, where $\dot{\alpha}$ is the pitch rate in rad/s, $\bar{c}$ is the mean aerodynamic chord, and U_∞ is the tunnel freestream velocity.

3. Effect of Yaw

As a UCAV operates under a wide range of wind conditions, it is susceptible to gust effects. Thus, it is important to document its behavior with side-slip. Through flow visualization, yaw maneuvers at zero angle of attack have been shown to mimic the steady flow cases as well as indicating the presence of strong side-slip. No other effects besides this side-slip were exhibited [3]. It is desirable however to study the pitch-up maneuver with nonzero yaw angles ($\beta \neq 0$). This would represent a maneuver in side wind and could even be used to investigate gust response, which tends to be an unsteady flow situation.

4. Effect of Leading Edge Curvature

Gursul et al. [4] have established that nonslender delta wing vortices are strongly affected by leading edge shape, particularly the attachment location. After the flow separates from the leading edge, it forms the previously mentioned leading edge vortex. Up to high angles of attack, however, the shear layer containing the vortex reattaches to the aircraft body and flow resumes along the surface. The line along the wing where the vortex reattaches is known as the attachment line. The primary vortex attachment line occurs outboard of the symmetry plane and moves inboard towards the centerline with increasing angle of attack [4]. As the attachment line moves inboard, stall onsets more

quickly. Gursul et al. studied a 50-degree swept wing and discovered that for rounder leading edges, the reattachment line is more outboard indicating a delay in the stall. Figure 5 shows one of their flow visualization pictures. In their study, they noticed that for any given angle of attack, a rounder leading edge shape produced a higher *y/s* or lower Θ, defined as shown in Figure 5.

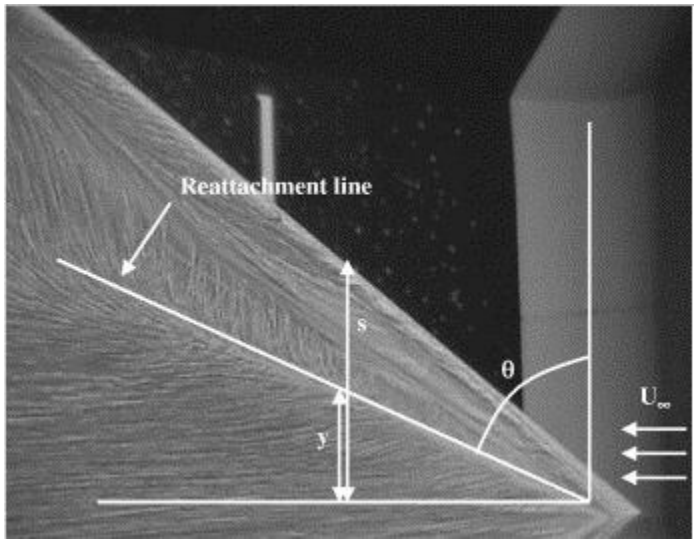

Figure 5. Flow Visualization of Attachment Line. From [4].

Miau et al. [15] conducted experiments over a similar wing shape at very low Reynolds numbers, and their conclusions also confirmed that leading edge shape had a significant effect on the flow field. They determined that the formation of the leading edge vortices was strongly affected by leading edge shape. Kawazoe et al. have demonstrated the same results for a rounded leading edge for a sweep angle of 45 degrees [16].

McParlin et al. presented the results of their steady flow experiments over the 1303 configuration. The previous studies regarding leading edge radius effects on slender delta wings motivated them to explore leading edge curvature effects on a UCAV 1303. They noticed a favorable Reynolds number effect on lift coefficient C_L at pitch angles

greater than 10 degrees for a rounded leading edge configuration. For the same shape, they also noticed a delay in the onset of pitch-up to a slightly higher angle of attack [9].

Ol also observed that when his model surface was painted for PIV and then again for flow visualization studies, his previously captured vortical structure had disappeared [13]. This may suggest that the surface geometry, perhaps due to incidental leading edge radius effects, could play a major role in low Reynolds number testing.

Thus, there is considerable evidence in the reported literature that leading edge plays a major role in altering the flow features of a nonslender delta wing, and it was deemed worthwhile to implement a suitable curvature change for the present UCAV 1303 geometry. This change was investigated to see if any beneficial effects, in particular elimination of tip-stall and a favorable enhancement of moment behavior could be achieved. The present research is aimed towards this goal.

C. GOALS OF THE PRESENT EXPERIMENTS

The motivation of the present experiments was therefore twofold. The first goal was to validate the flow visualization and load measurement results previously attained, as well as to take advantage of the benefits already noticed of a rounded leading edge. It was important to verify and reproduce steady flow data in order to prove the current model comparable. Once validated, unsteady flow data was collected at varying angles of yaw and repeated with a modified leading edge. For ease of comparison, the original model leading edge radius of 1/64 inch was doubled cylindrically to 1/32 inch.

By modifying the vortical flow, the dynamic stall effects could potentially be enhanced in order to develop a wider flight envelope. Also, by gaining a proper understanding of the maneuver characteristics in yaw, the control systems can be modified to appropriately and safely operate the UCAV in varying winds. In contrast, a rounded leading edge may have had very adverse effects on other moments or forces which could be detrimental to other parts of the flight pattern. These effects were also important to document before any tests are done at a larger scale.

THIS PAGE INTENTIONALLY LEFT BLANK

II. EXPERIMENTAL FACILITY AND TECHNIQUES

A. THE NPS WATER TUNNEL

1. Overview

The flow visualization and load measurements featured throughout the report were all performed in the Naval Postgraduate School's (NPS) Water Tunnel Facility. The Rolling Hills Research Corporation (RHRC) Model 1520 Water Tunnel is a closed circuit, continuous flow facility suitable for studying a wide range of aerodynamic and fluid dynamic phenomena. An image of the water tunnel is featured in Figure 6.

Figure 6. RHRC Water Tunnel Model 1520. From [17].

The horizontal configuration of this tunnel allows for visualization from the sides and bottom of the test section, and axially through a downstream transverse window, while dye is injected into the flow from six different canisters installed on the side of the tunnel. The water tunnel operates in a closed circuit mode. The test section is 15 inches wide, 20 inches high, and 60 inches long and is constructed of tempered glass allowing

for maximum viewing. The test section is also slightly divergent to compensate for boundary layer growth during operation [17].

The level of flow quality up to 15 inches per second flow velocity in the test section is reported by [17] as the following:

- Turbulence Intensity Level: < 1.0% RMS
- Velocity Uniformity: < ±2.0%
- Mean Flow Angularity: ≤ ±1.0° in both pitch and yaw angle

A temperature probe placed in the test section is utilized to record the water temperature. The information is also used to accurately compute the dynamic pressure which is necessary for normalizing the aerodynamic coefficients.

2. Model Support

The model is held in the test section utilizing a computer controlled model support system. This system, shown as Figure 7, is capable of complex motions including forced oscillations, specific maneuvers, and rotary balance motions. Dynamic motion cases of scaled vehicles at appropriate non-dimensional rates make the results applicable to practical systems.

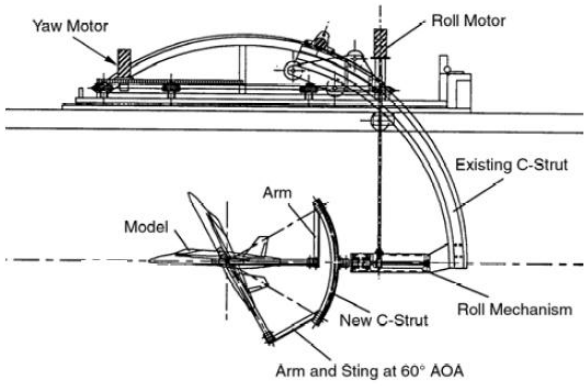

Figure 7. C-Strut Model Support System. From [17].

The system allows control for steady roll, yaw, and pitch angles as well as many types of dynamic operations. The model is supported from the top using a C-strut to

change pitch angle and a turntable to change yaw angle; both of these motions have their own remotely driven DC motor. A third motor is enclosed in a waterproofed mechanism which supports roll motions. The model is supported in the inverted position in order to avoid free surface effects. In this way, a traditional nose-down orientation is actually a nose-up attitude. The data acquisition system for load balance studies allows for appropriate tares to be taken in order to negate any gravity effects that are the only significant aspect for this research. As configured in the NPS Water Tunnel, the model is capable of the following motions: -1° to 40° pitch-up, ±360° roll, and ±30° yaw. The entire system, from tunnel velocity to model motion, is driven by a PC based LabVIEW software.

B. THE UCAV 1303 MODEL

In order to perform a flow visualization study as well as a load study, two 1/72-scale UCAV 1303 models were used. The Air Force Research Laboratory (AFRL) provided the CAD file for the geometries tested. The model includes a fuselage, but it does not include engine flow simulations. They were fabricated out of nylon 12 PA using rapid prototyping techniques and coated with polyurethane to produce a smooth exterior necessary for aerodynamic testing. Its dimensions are given in Table 1. The dimensions correspond to a scale ratio of 1:72 and thus, reproduction of the fine scale detail—such as leading edge curvature—is limited only by the manufacturing process [1]. The first model houses several dye ports along the leading edge to inject flow tracing to generate flow visualization images of the various phenomena that occur over this airfoil. There are four, 0.6 millimeter ports per side that are located at 5, 11, 22, and 33 percent root cord respectively. Additionally, dye was introduced externally through a tube so that flow off of the wing surface could be visualized. Two digital cameras were used to record the images from beneath and beside the tunnel to observe the flow over wing surface. This model is shown in Figure 8.

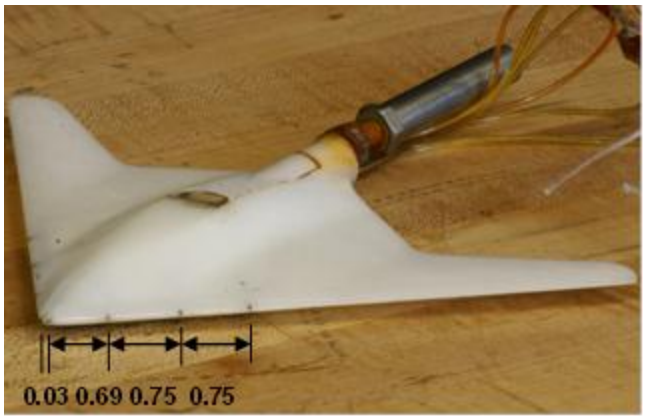

Figure 8. UCAV 1303 Model with Dye Ports (Distances along Leading Edge in Inches). From [1].

The second model houses a very sensitive, submersible, five-component submersible internal strain gage balance which captures very sensitive load data for calculations of the following: normal force (N), side force (S), pitching moment (PM), rolling moment (RM), and yawing moment (YM). The models are identical in area, span, and mean aerodynamic chord (MAC); their measurements are tabulated in Table 1 and depicted in Figure 9.

Table 1. Model Properties. From [3].

Property	**Value**
Reference Area (A_{ref})	21.11 in^2
Wing Span (b)	9.00 in
Root Chord (c)	5.24 in
Mean Aerodynamic Chord ($\overline{c}$)	3.54 in

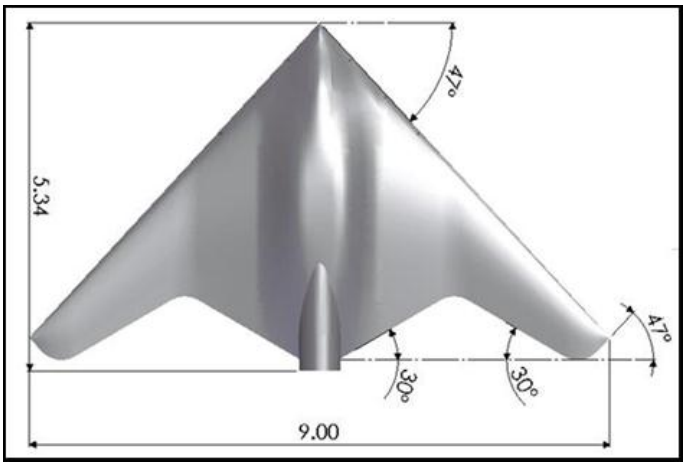

Figure 9. UCAV 1303 Model with Dimensions (Inches). From [1].

C. LEADING EDGE MODIFICATION

As stated earlier, leading edge curvature effects have the most significant influence on the flow features. Thus, the present studies required leading edge modifications. Also, it is not practical to make multiple models, each with a different wing leading edge curvature. It is thus clear that for this purpose, the simplest and most repeatable solution was desired. Several attempts were made in this regard. The first attempt was with common, shapeable, crafting materials such as Sticky Tack and commercially available clay. It became quickly apparent that these were not satisfactory because they were unsuitable for use in water and also never could be cured to the required degree of hardness to retain the shape to which they were formed.

Next, a small, rubber tube was attached over the leading edge. The radius could be easily measured and changed, simply by replacing the tube with a different one. This method, however, left an unacceptable step from the tube to the model body. The step created an undesirable recirculation just behind the leading edge that carried flow from the apex towards the wing tips. A typical result can be seen in the flow visualization images, one such is shown in Figure 10.

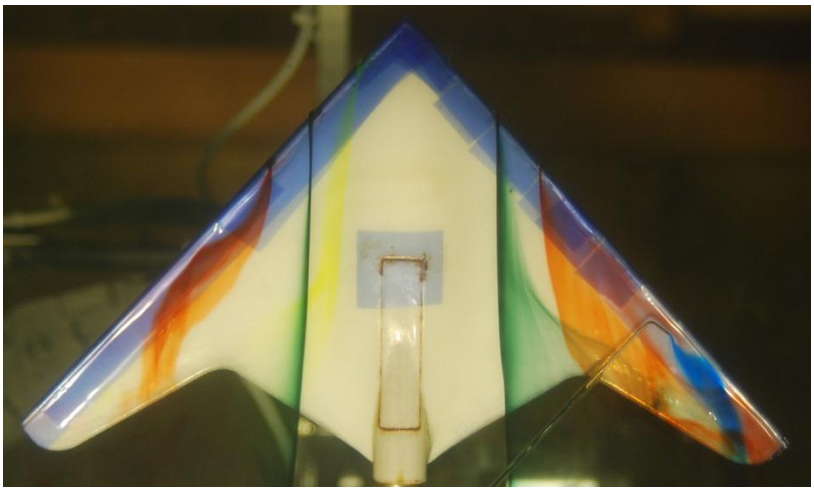

Figure 10. A Small Rubber Tube Placed over the Leading Edge Creates An Undesirable Recirculation Zone. Re = 1.3 x 10^4, Steady Flow, $\alpha = 5°$.

In order to overcome this step, attempts were made to use metal shims since they could be extended onto the wing and fuselage to merge with them more aerodynamically and smoothly as indicated in Figure 11.

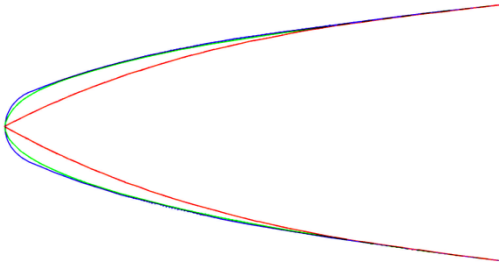

Figure 11. An Example of a Leading Edge Modification Blending into the Body. From [9].

The metal shims, however, could not properly retain the radius of curvature due to the softness of the metals from which the shims are constructed.

The final solution was to custom cast a fiberglass attachment. This was an extremely lightweight, thin solution that fitted as a glove over the wing leading edge. The leading edge could be fabricated to the desired radius with accuracy, and a similar cast could be created easily for reproduction of the results with a different radius. The test

data reported here were generated for a new leading edge radius of 1/32 inch, which is twice that of the 1/64 inch value for the baseline wing. Also, the custom fiberglass cast blends into the rest of the body for a more realistic design application without increasing the overall planform area. The attachment is an average of 0.762 millimeters thick representing 10% of the model thickness and is shown in Figure 12.

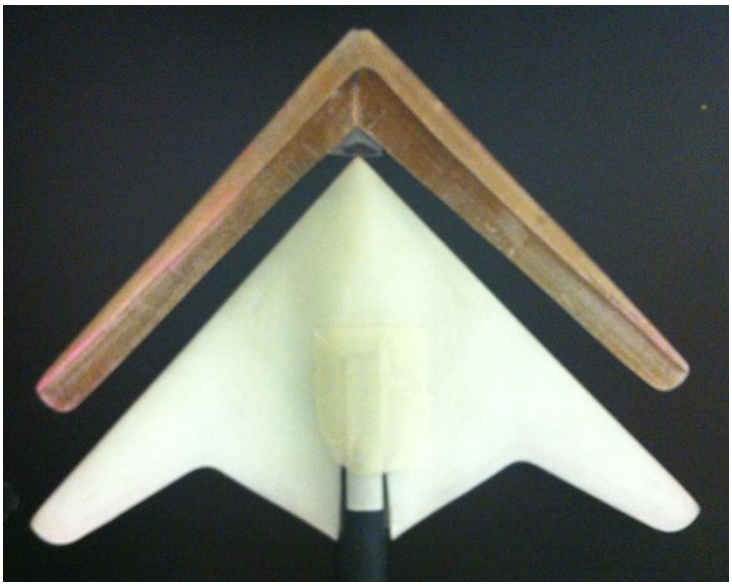

Figure 12. The Fiberglass Attachment Constructed placed in front of the Load Model.

D. INSTRUMENTATION

1. Water Tunnel Software

RHRC provides a comprehensive LabVIEW program to remotely control the water tunnel. This program displays both the balance and tunnel condition data so that the user can properly monitor the experiment. The program also acquires data during both static and dynamic experiments, which is processed using a previously recorded tare file and reduced for plotting and further analysis. Data is acquired and reduced using standard methods for both steady and unsteady flow experiments. For the latter, it is critical to define a model motion history and repeat it as many times as necessary for achieving statistical stationarity of the data. These details are conveniently implemented in the

DAQ software. The programmed experiments are fully adjustable, from water speed to model motion to data sampling rates. The raw data can be packaged for plotting in a format readable by both Excel and MATLAB.

2. Load Measurement

A five-component strain gage balance is attached to the sting in order to measure the loads developed by the model. The gages and sting are then consequently shrink wrapped and covered with several layers of Room Temperature Vulcanization (RTV) silicone. This ensures a watertight seal and reliable operation in the water tunnel. Each channel is connected through a full Wheatstone bridge, and external resistors compensate for both the gage resistance and temperature variation. A potentiometer, balances the strain gage externally [17]. Figure 13 shows the Wheatstone bridge, and Table 2 lists the resistor values used. The strain gage voltages filtered and amplified using programmable National Instruments signal conditioners before processing for obtaining the force and moment coefficients.

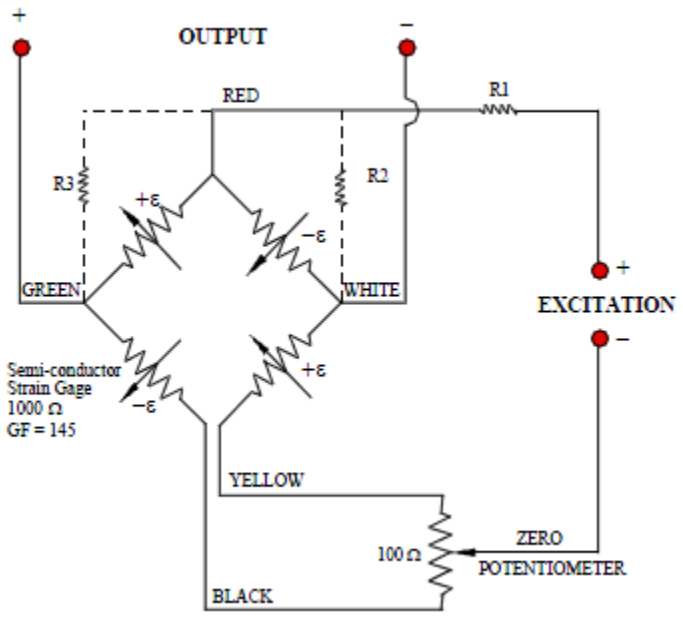

Figure 13. Wheatstone Bridge Circuit. From [12].

Table 2. Resistor Values used in Strain Gage Bridge Circuit. From [12].

Channel	R1	R2	R3
CH1 (YM1)	1k Ω	0 Ω	458.7k Ω
CH2 (PM1)	1k Ω	0 Ω	152.5k Ω
CH3 (RM)	1k Ω	0 Ω	756.5k Ω
CH4 (PM2)	1k Ω	0 Ω	38.8k Ω
CH5 (YM2)	1k Ω	0 Ω	351.3k Ω

They are fit with a 1000 ohm semiconductor and are calibrated to a maximum of 0.22 pounds. Table 3 lists the sensitivities of each quantity.

Table 3. Strain Gage Sensitivities. From [12].

Force/Moment	Sensitivity
N	2.4 V/lb
S	16.8 V/lb
PM	5.0 V/in-lb
RM	10.2 V/in-lb
YM	16.4 V/in-lb

The five components measured are the following: pitching moment coefficient (C_M), yawing moment coefficient (C_{YM}), rolling moment coefficient (C_{RM}), as well as normal force coefficient (C_N) and side force coefficient (C_S).

3. Flow Visualization

Flow visualization was conducted using water-soluble food coloring. The coloring was premixed with water in a ratio of 1:4 in order to maintain neutral buoyancy in the flow field. The colored mixtures were stored in pressurized canisters and routed through

individual lines to the model's dye ports. In this experiment, the dye was split symmetrically between the port and starboard sides.

Controlling the dye's flow rates was particularly important. Experimental investigation showed that large flow rates pushed the dye away from the surface. It was necessary to inject enough dye at near zero momentum from each outlet [3]. This yielded results which could not only be easily analyzed, but also enabled proper interpretation of the near surface flow field.

E. DESCRIPTION OF THE EXPERIMENT

Both steady and unsteady flow data were obtained. Before the experimental run could be performed, however, several precautions needed to be taken. It was very important that the model be in a well-defined "zero-position." This created a consistency between experiments which increased the confidence of comparison between them. The pitch and roll planes were zeroed by using a small spirit level placed on the undercarriage (top-facing surface in the water tunnel). The yaw plane was zeroed by aligning the model support system's C-strut with a premeasured mark on the rig.

For each, the software then performs a five point tare which is used in conjunction with the measurements taken during the experiment in order to calculate the actual loads and moments. Since the model support is less bulky than similar wind tunnel supports, the only tare to be removed is the gravity tare. For static runs, it is necessary to establish a satisfactory settling time prior to data acquisition for obtaining statistically steady results. This is because the inertia of water is large, and any model movement causes a large disturbance in the flow. After consultation with RHRC, an experiment was conducted in steady flow at U_∞ = 10 in/sec (Re = 2.3 x 10^4). The model was pitched through an angle of attack from 0 to 30 degrees in two separate runs. The first run had a two minute acquisition period after a settling time of two minutes, and the second run acquired data over 40 seconds after 15 seconds of settling time. Figure 14 shows the results of normal force variation with angle of attack that was recorded. The excellent agreement between the two cases clearly suggests that the shorter settling time of 15 seconds is satisfactory and hence, was used for all subsequent experiments.

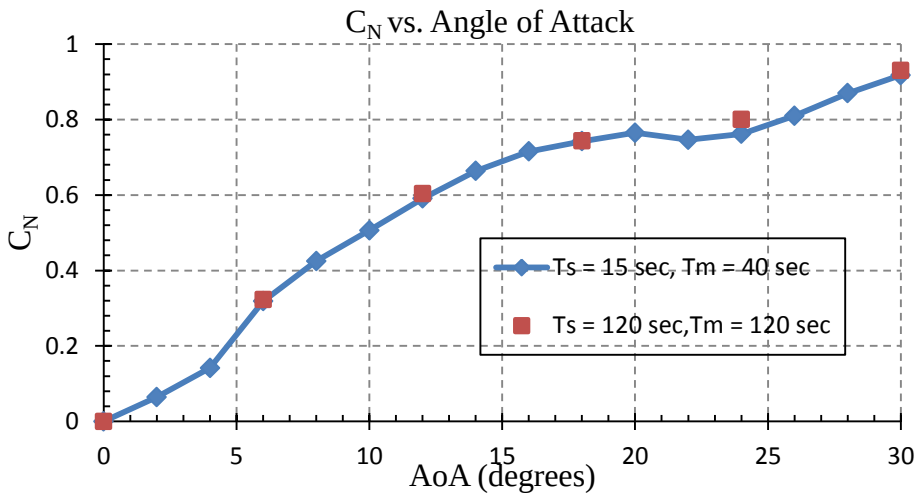

Figure 14. Variation of Normal Force Coefficient with Angle of Attack and Data Acquisition Times. Re = 2.3 x 10^4, steady flow.

Dynamic runs were performed using a ramp-up pitch motion. For each case studied, the model was cycled through the motion 20 times at a data collection rate of 60 Hz. Similar to the settling time in the static data, an analysis needed to be done on how many cycles would be necessary to get statistically stable data. An analysis of previous data taken over 100 cycles showed that there is negligible effect passed 20 cycles [12]. At 60 Hz, the 20 cycles yield over a minimum of 20,000 lines of information at varying angles of attack. Since there will be cycle-to-cycle variations, it is necessary to group the data into small bins and perform statistical analysis for each bin separately. Specifically, ensemble averages were computed after grouping the data into 0.5 degree AoA bins for statistically accurate analysis. A typical sample of the model's motion during a dynamic run is shown in Figure 15.

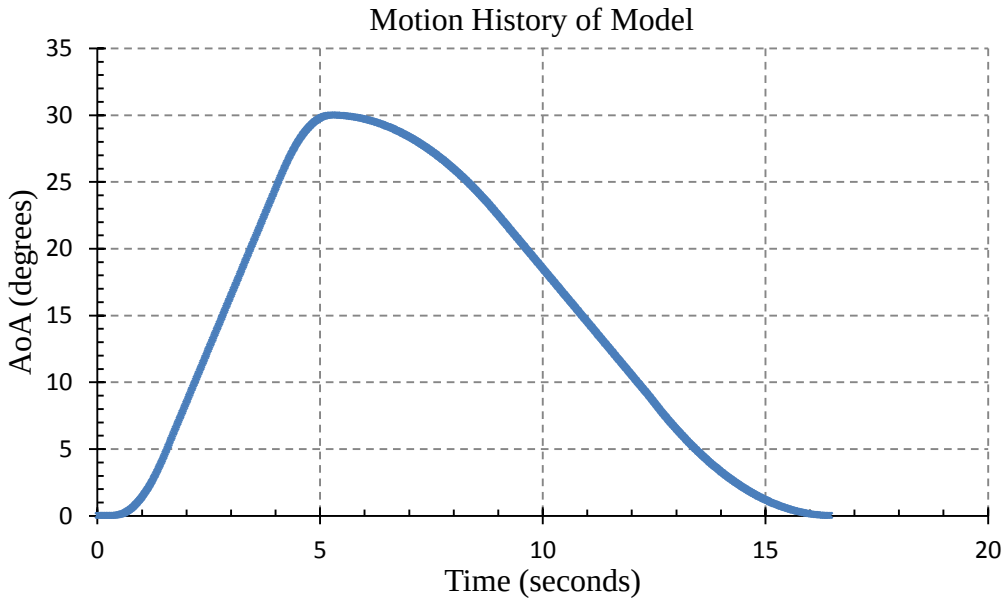

Figure 15. Example Motion History of Model. Unsteady Flow, Re = 2.3 x 10^4, $\alpha+ = 0.05$.

F. EXPERIMENT MATRIX

The experiments were conducted for the conditions in Table 4.

Table 4. Experimental Conditions. After [1].

U_∞	6 [in/sec]	10 [in/sec]	14 [in/sec]
Re	1.3 x 10^4	2.3 x 10^4	3.1 x 10^4
Pitch Angles, α	0°-30°	0°-30°	0°-30°
α^+	0.00, 0.05, 0.10	0.00, 0.05, 0.10	0.00, 0.05
$\Delta\alpha$	2°	2°	2°
Yaw Angles, β	0°-6°	0°-6°	0°-6°
$\Delta\beta$	2°	2°	2°
$\beta+$	0	0	0

G. MEASUREMENT UNCERTAINTY

The experimental uncertainties were estimated in the usual manner by including the uncertainties in each major component that forms the quantity measured and are listed in Table 5. It is also noted here that the loads measured are sometimes as low as milligrams as a result of the small dynamic pressures produced by the low-speed water tunnel. The discrepancies in plots are therefore less significant than they appear. Thus, there may be greater uncertainty in certain quantities than normal force or pitching moment.

Table 5. Measurement Uncertainties. From [12].

Parameter or coefficient	% Uncertainty
U_∞	± 4 %
ρ	± 0.2 %
Normal Force	± 2 %
Side Force	± 0.5 %
Moments	± 1 %
C_N	± 5 %
C_M	± 3 %
C_S	± 1 %
C_{YM}	± 3 %
C_{RM}	± 3 %

THIS PAGE INTENTIONALLY LEFT BLANK

III. RESULTS

A. VALIDATION OF EXPERIMENTAL RESULTS

In order to validate the results of the present work, a small sample of initial results was compared with [12]. The normal force coefficient plot from a static run (α = 0–30°) performed at Re = 2.3 x 10^4 is shown in Figure 16. Given that the flow separates at a very low angle of attack, some differences are bound to appear. Overall, the agreement is quite good. It is noted here that the maximum difference measured in these two cases is about 1/8 ounce, around the unsteady tip-stall angle, which is within the estimated uncertainty of the measurement. This plot shows that tip-stall is still observed at the lower angles of attack around five degrees. It also shows the same trends of vortex formation, breakdown, and bursting between the approximate angles of 16 and 22. Finally, the normal force coefficient plot exhibits the same range, with a maximum value of 0.80 for both cases. These values are also consistent with published literature [9], which were obtained at a higher Reynolds numbers and Mach numbers. Figure 17 shows the variation of the pitching moment coefficient for the same run. Although slightly different values are recorded—a difference attributanle to small values of the measured forces encountered in the water tunnel—qualitatively, a clear comparison can be seen. Pitch-break is still a major issue around the same angle as tip-stall and so is the effect of the vortexl formation and breakdown. However, the data are internally consistent that they are repeatable within each operator with similar differences and follow the same trends.

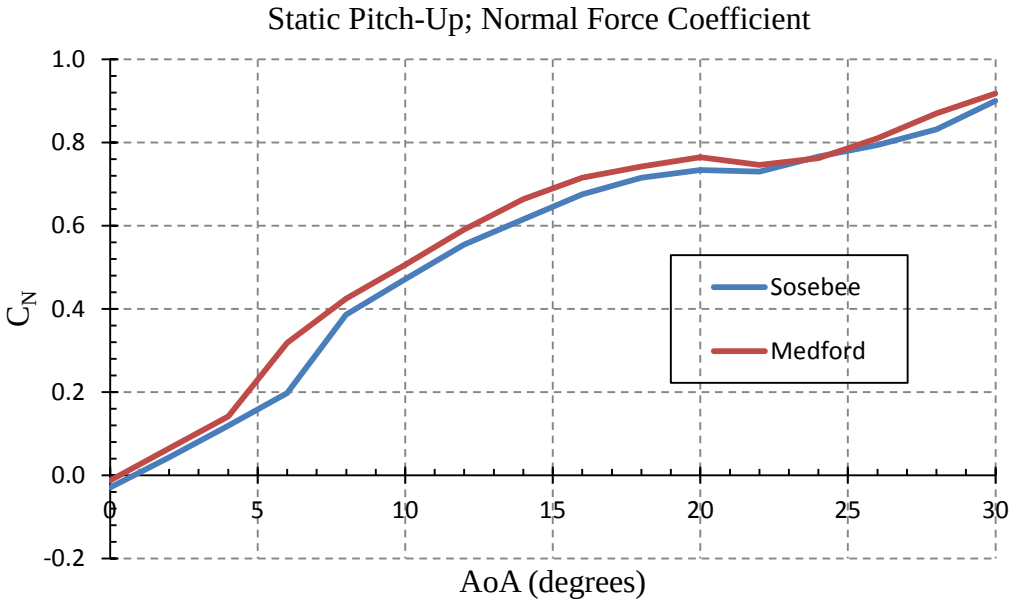

Figure 16. Comparison of C_N in Present Static Work. After [12].

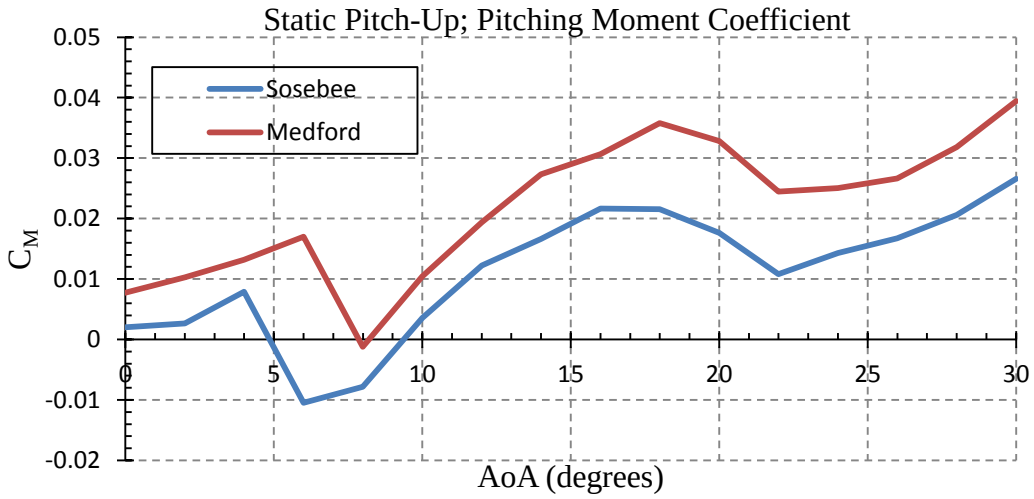

Figure 17. Comparison of C_M in Present Static Work. After [12].

The normal force coefficient plot from a dynamic run (α = 0–30°, α+ = 0.05) performed at Re = 2.3 x 10^4 is shown in Figure 18. The closeness of results is once again within the above discussed variability and validates the methodology used in the experiments is valid. Both demonstrate production of dynamic lift and smooth, linear trends from near-zero to a maximum value of around 1.4.

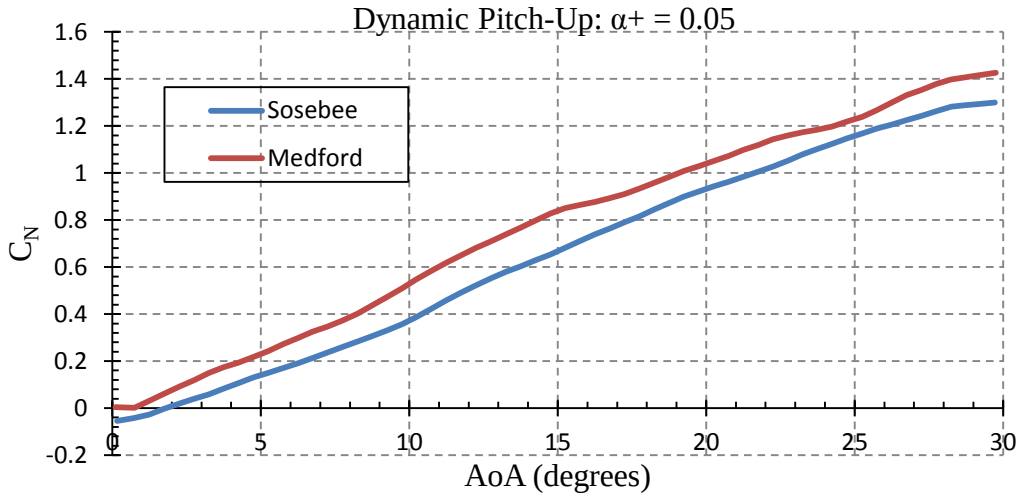

Figure 18. Comparison of C_N in Present Dynamic Work. After [12].

With these initial runs reproducing the earlier results closely and resembling the trends in previous literature, the measurements were deemed valid to proceed.

B. EFFECT OF REYNOLDS NUMBER

1. Static Load Measurement Studies

In order to study the effects of Reynolds number on the UCAV 1303, initial tests were performed where the water tunnel velocity was increased from 6 [in/sec] to 10 [in/sec] to 14 [in/sec]. These speeds correlate to Re = 1.3 x 10^4, 2.3 x 10^4, and 3.1 x 10^4, respectively, and are also representative of the studies performed by McLain [3] and Sosebee [12]. Incidence was increased at intervals of 2 degrees from 0–30 degrees.

The resulting C_N and C_M plots are shown in Figure 19. It is evident that the C_N curve is nonlinear at all Reynolds numbers, which is different than what is seen for most conventional geometries. A break in the C_N with α curve is seen for all three cases studied at very low angles of attack. At Re = 1.3 x 10^4 (blue diamonds), the deviation occurs around 6 degrees and only slightly breaks the trend. The break systematically moves to lower angles of attack as Reynolds number increases. At Re = 3.1 x 10^4 (green triangles and the highest Reynolds number tested), the break is stronger and seems to stabilize at around 2 degrees. This break in the C_N curve is associated with the occurrence

of tip-stall. The onset of tip-stall has been explained in [1] and is due to the vortex in the trailing edge crank wake breaking up and spreading the flow sideward, forcing it to move upstream near both (see also Figure 3) wing tips. A review of the literature confirms that tip-stall has been observed at higher Reynolds numbers and Mach numbers, in both experimental and computational studies. Thus, it can be said that a water tunnel study, despite the lower Reynolds numbers, reproduces the physical flow details and effects satisfactorily. As the angle of attack is increased, the changing flow details over the main wings will once again restore the flow to its normal state and the normal force re-develops, ending the pitch-break seen.

The vortical flow described earlier in Section I.B develops as the wing is pitched past these angles. The formation angle depends slightly on the Reynolds number, however, it is around 10 degrees. The process is gradual unlike that seen in a slender delta wing, where the entire leading edge shear layer rolls-up, causing a strong low pressure in the vortex core, causing a sudden lift increase. Likewise, the break up is also gradual, and it progresses towards the wing apex with increasing angle of attack. Thus, the loss of lift appears as gradual loss, like that seen in trailing edge stalling airfoils.

As can be expected, such variations in the pressure field of the wing also induce pitching moment variations, which is relevant to the longitudinal stability of the UCAV model. The corresponding C_M plots are presented in the bottom half of Figure 19. The normal force break, due to its abrupt nature, translates to a break in the pitching moment at the same angle. In fact, even if the breaks are subtle in C_N, they appear sharper in C_M and hence, pitch-breaks serve as a better indicator of the tip-stall occurrence. Incidentally, even though it seems that C_M decreases briefly with α, making $dC_M/d\alpha$ negative, the lack of flow over the wing tips and surrounding appendage makes controlling the UCAV a challenge. Thus, a pitch-break is not desirable and needs to be softened at a minimum. The flow recovery beyond this point re-establishes the flow, however, adding a further complexity in that the C_M rises with α, making the UCAV longitudinally increasingly unstable as the angle of attack is increased, until the vortex burst phase. Although these

results are similar to those reported by others, so far no proper solution has been proposed and this study attempts to offer one which will be discussed in Section F.

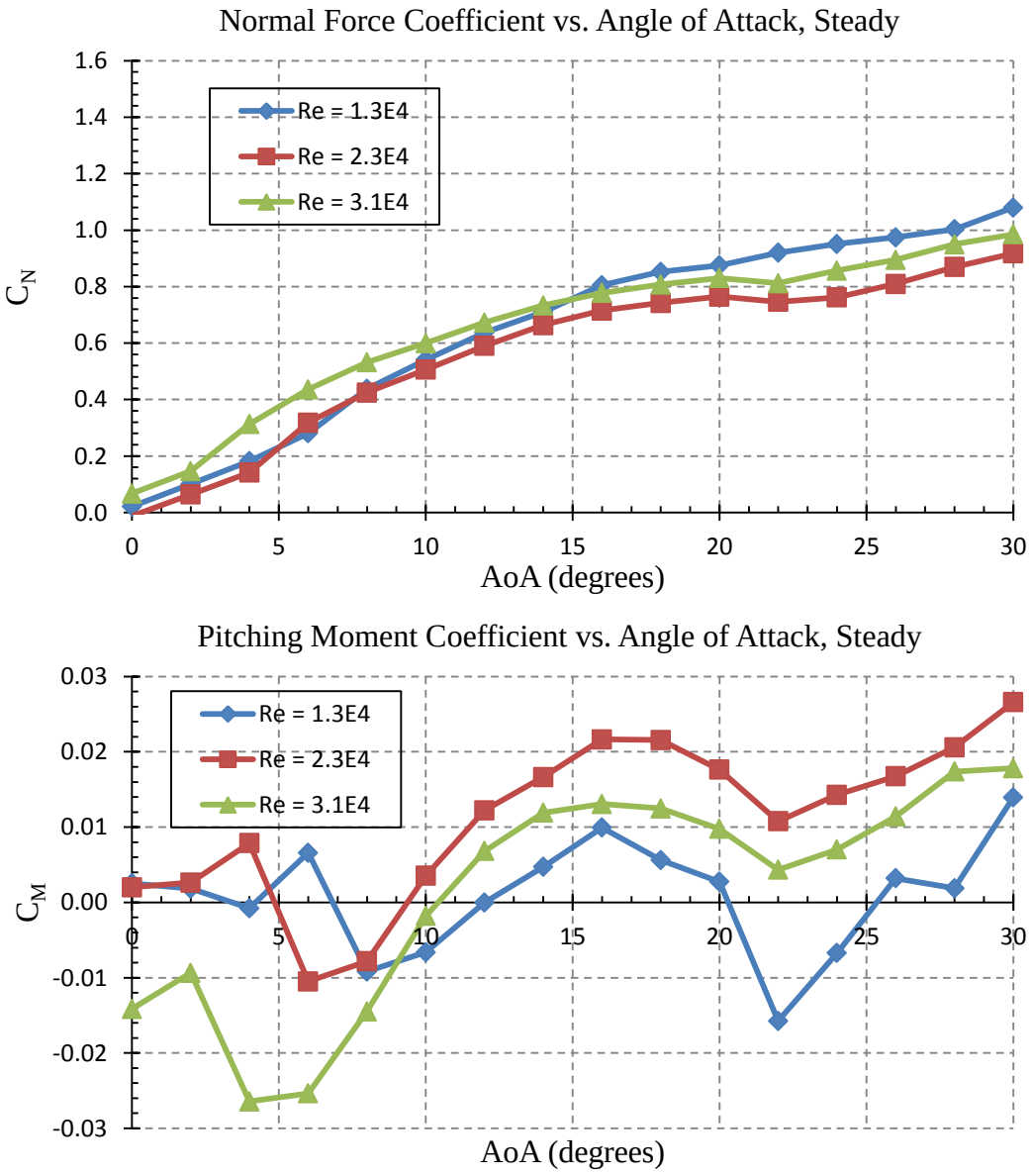

Figure 19. Reynolds Number Effects on C_N and C_M; Steady Flow.

Figure 20 shows the resulting C_S, C_{YM}, and C_{RM} plots, which at almost all Reynolds numbers and angles of attack are near zero. Any small departures seen at low angles of

attack from the expected value is once again attributable to the overall small range of values encountered and the difficulties in measuring those. The side force is steady (and near zero) until higher angles of attack are attained. The vortical flow at the higher angles which was discussed earlier can be expected to induce additional side forces and moments, but even these have been consistently found to be small. Since others have not studied these quantities, it is not possible to provide any other comparisons. The importance of not suffering from flow induced side forces and yawing moments is critical since the UCAV 1303 is a tailless aircraft and therefore has no vertical rudder to easily offset the longitudinal effects.

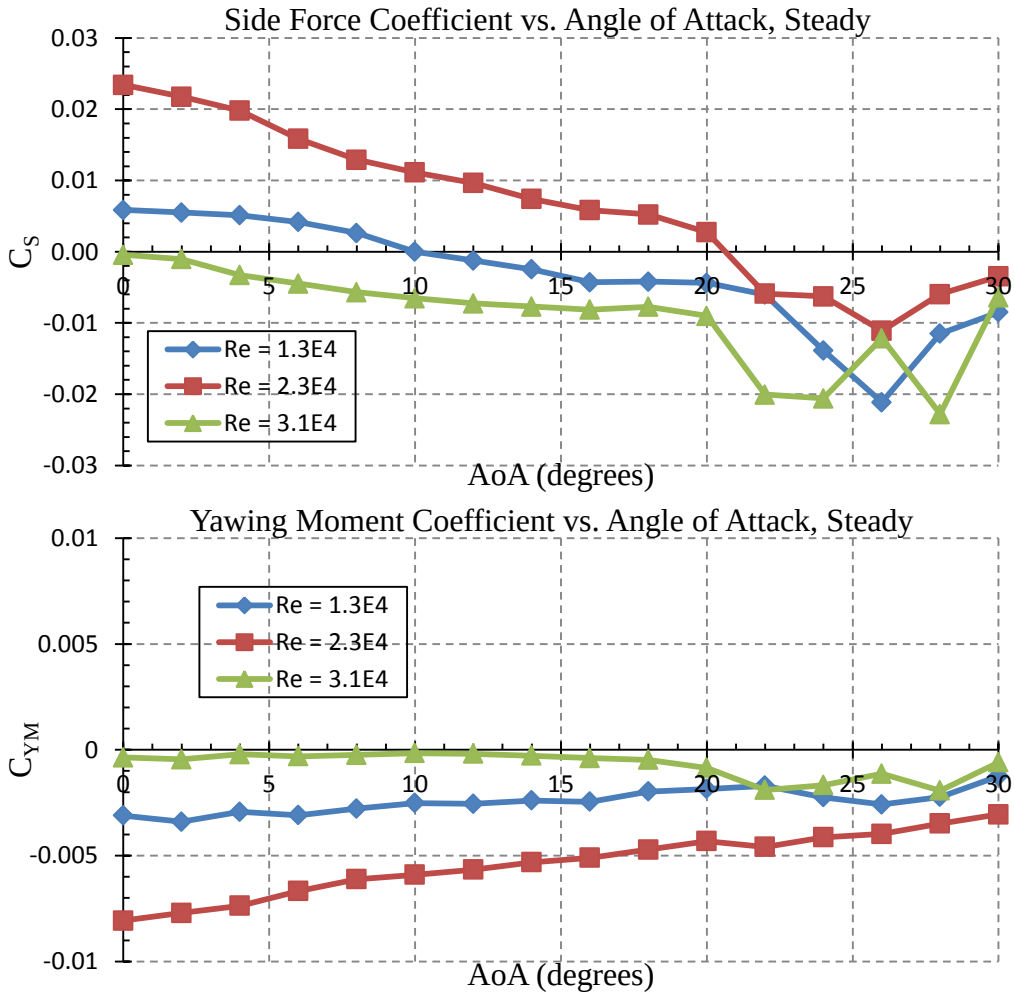

Figure 20. Reynolds Number Effects on C_S, C_{YM}, and C_{RM}; Steady Flow (continued on next page).

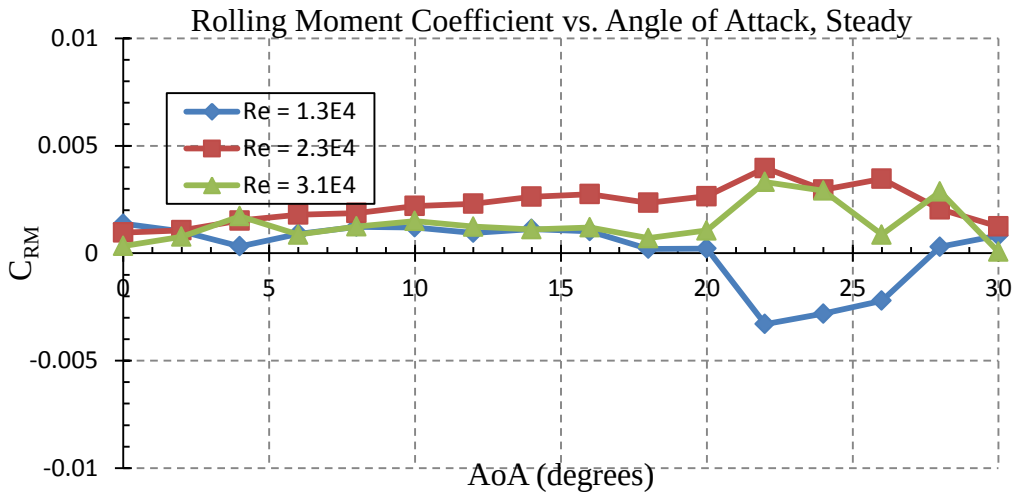

Figure 20. (Continued) Reynolds Number Effects on CS, CYM, and CRM; Steady Flow.

2. Dynamic Load Measurement Studies

For ease of comparison, the dynamic measurements examined in this section were all performed at $\alpha+ = 0.05$, with a range of incidence from 0–30 degrees. Figure 21 shows the effect of Reynolds number on C_N, C_M, C_S, C_{YM}, and C_{RM}. It is evident that when the aircraft is maneuvering, Reynolds number has little effect. In all cases, the values recorded are of similar value. The difference, however, is that at higher Reynolds numbers, the curves are much smoother. For example, at Re = 1.3 x 10^4 (the blue line), readings are more sporadic. This is a result of many weaker vortices forming and bursting asymmetrically. At the higher Reynolds numbers (green and red lines), the vortices that form are stronger and more consistent, driving a smoother curve. Dynamic studies will be looked at even closer with the varying pitch rates. The rapid pitch up maneuver also has eliminated the tip-stall effects observed in steady flow and so, no breaks are seen in the C_N distributions, a fact that the flow visualization data [1] also supports. This also manifests as smoother C_M distributions and the rise in C_M starts only after the vortical flow develops in the unsteady case. Since over the range of angles studied, the vortex did not exhibit a breakdown, both C_N and C_M are smoother compared to their steady flow counterparts. The effects of the pitch rate to be discussed further expand on this.

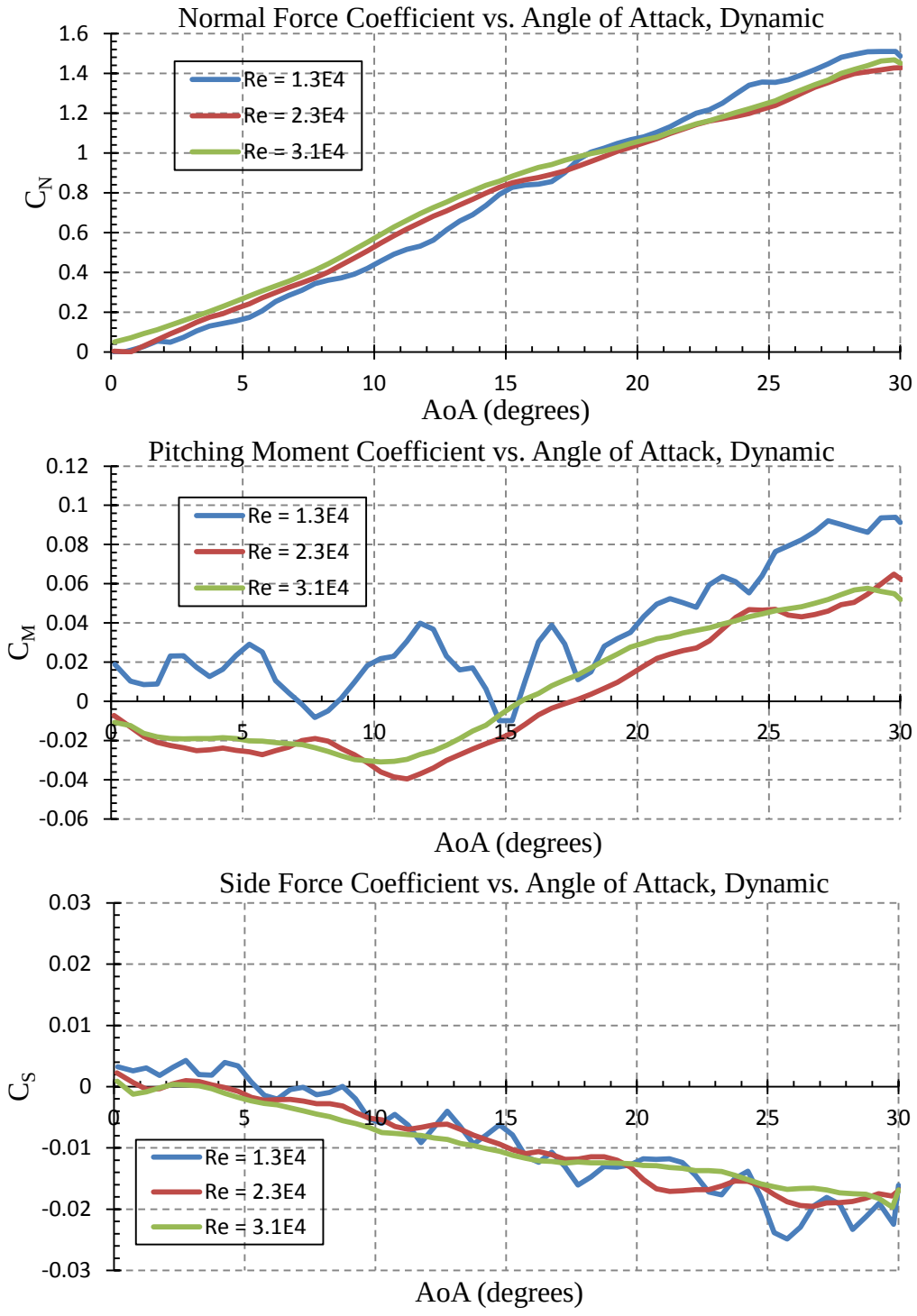

Figure 21. Reynolds Number Effects on Pitch-Up Motions (continued on next page).

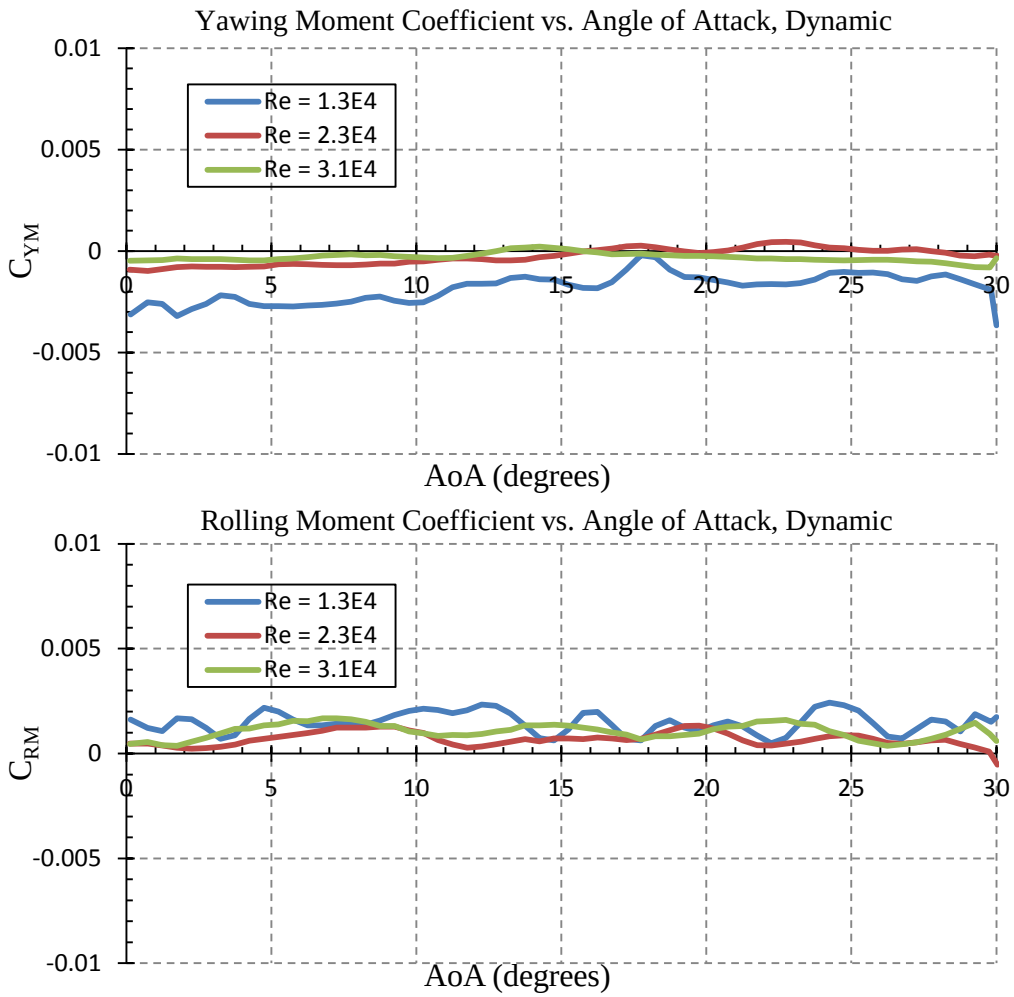

Figure 21. (Continued) Reynolds Number Effects on Pitch-Up Motions.

C. EFFECT OF PITCH RATE

Pitch rate can greatly affect the performance of a maneuvering aircraft. Aside from the static case ($\alpha+ = 0$), two other pitch rates were investigated: $\alpha+ = 0.05$ and $\alpha+ = 0.10$. The effect of pitch rate is shown in Figure 22. The middle Reynolds number tested is used for this comparison, however, the other two flow rates showed similar trends.

It is clear from Figure 22 that a pitch-up maneuver has alleviated tip-stall and a near 55% lift increment has been recorded at 30 degrees angle of attack. In this particular case, the normal force continues to grow linearly with angle of attack. Interestingly, no normal force breaks were observed both in flow visualization and in force data, indicating

that tip-stall does not occur in the dynamic motion case. This shows that the flow and subsequent vortices stay attached much longer than in the steady case. Flow visualization by [3] supports this because the vortex bursting location is shown to be farther back on the fuselage.

It was also observed in the case of pitching moment coefficient that the lines become smoother in the critical region of 0–10 degrees which confirms the absence of tip-stall. Also, the continued attachment of the vortices has caused a rapid rise in the pitching moment coefficient for both dynamic cases shown. In C_M plot, it is seen that a rapid pitching is preferred over a slower maneuver. This is manifested in the delay of the final rising of the curve. For the $\alpha+ = 0.05$ case, the coefficient ramps up at around 11 degrees, and in the $\alpha+ = 0.10$ case, the coefficient only takes off at around 18 degrees.

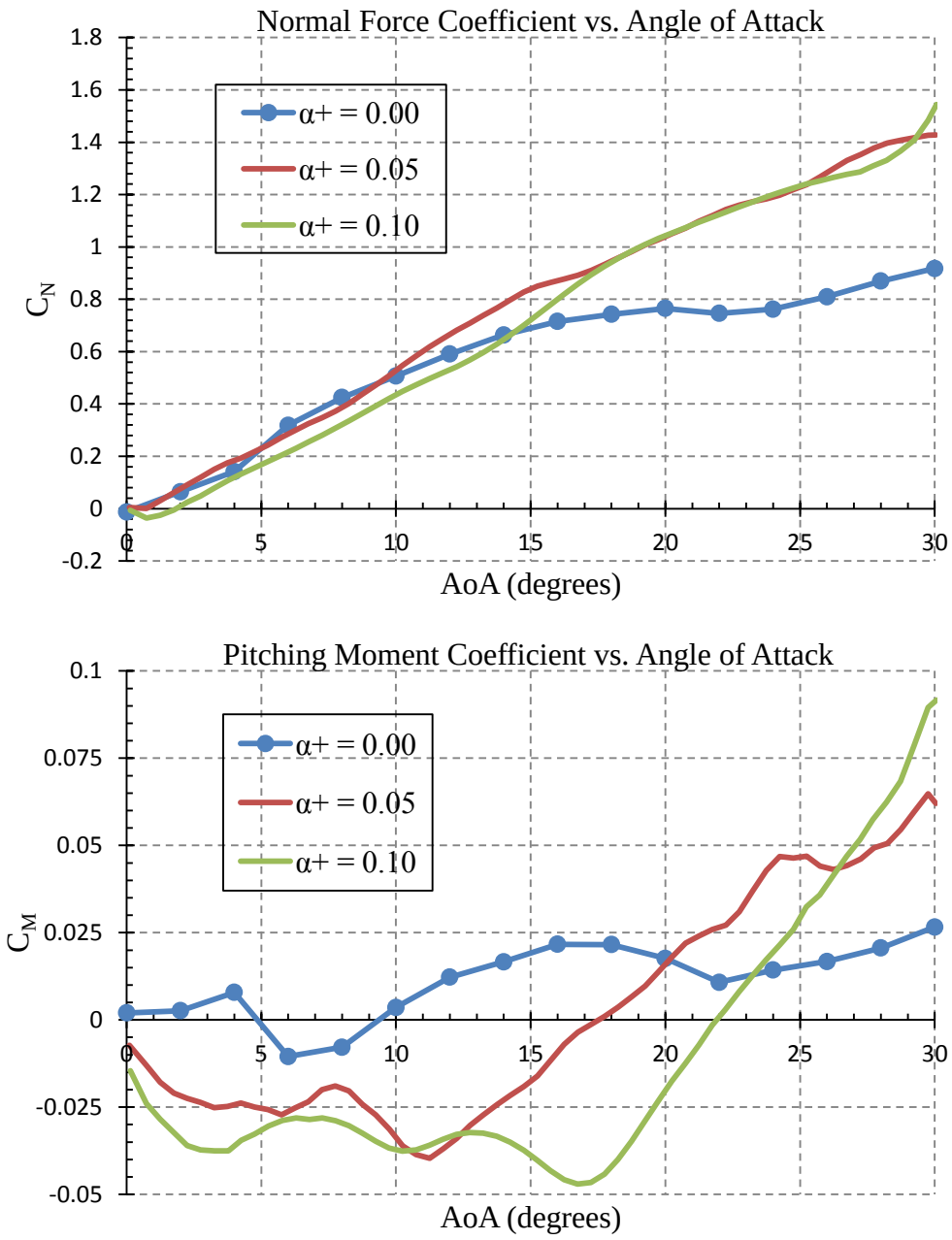

Figure 22. Variation of Normal Force Coefficient (top) and Pitching Moment Coefficient (bottom) with Pitch Rate, Re = 2.3 x 10^4.

Figure 21 shows that a pitch-up maneuver does not create any undesirable variations in the other forces and moments.

D. EFFECT OF YAW DURING MANEUVER

The effects of yaw angle (0, 2, 4, and 6 degrees) were studied in both steady and unsteady flow. Similar to the other results shown above, this test was largely unaffected by Reynolds number, and the middle flow rate is therefore chosen for comparison.

1. Static Load Measurements

Figure 23 shows the effect of yaw on normal force distributions. Despite local flow differences, tip-stall occurs at about the same angle of attack, 4 degrees. Small differences appear in C_N only after an angle of attack of 12 degrees. Although one could expect to see an influence of the asymmetrical vortices that form in these cases, they do not seem to affect the C_N values; however, a systematic shift can be seen in the side forces and rolling moment coefficients.

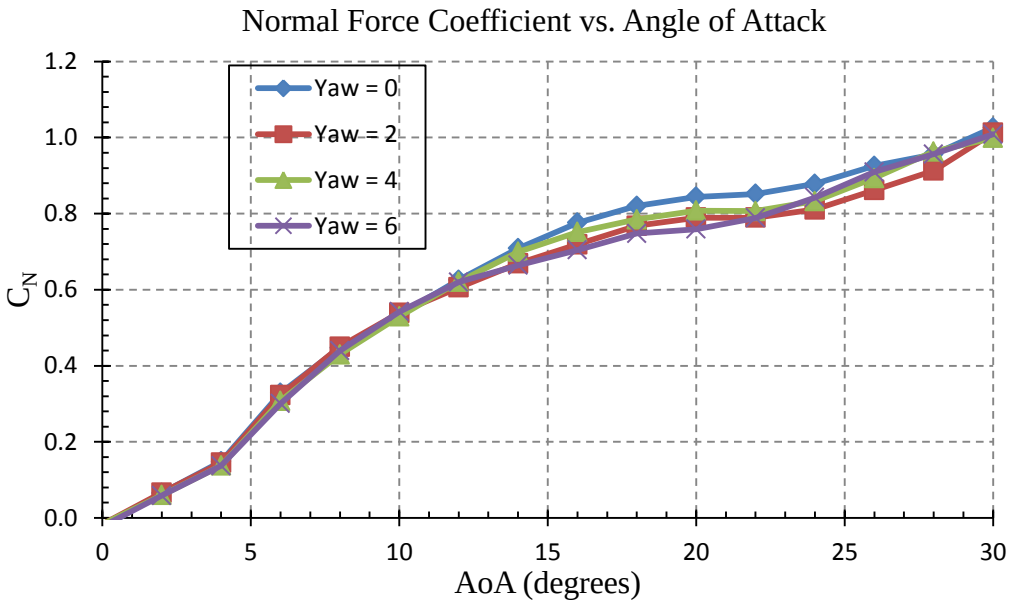

Figure 23. Yaw Angle Effects on Normal Force Coefficient, Steady Flow, Re = 2.3 x 10^4.

Figure 24 contains the C_M curve, which, similar to the C_N, exhibits the relatively same trend for all yaw angles. The pitch-breaks associated with tip-stall are again noticed at 4 degrees, and the only differences are only the small offset values which could be attributed to slight flow differences.

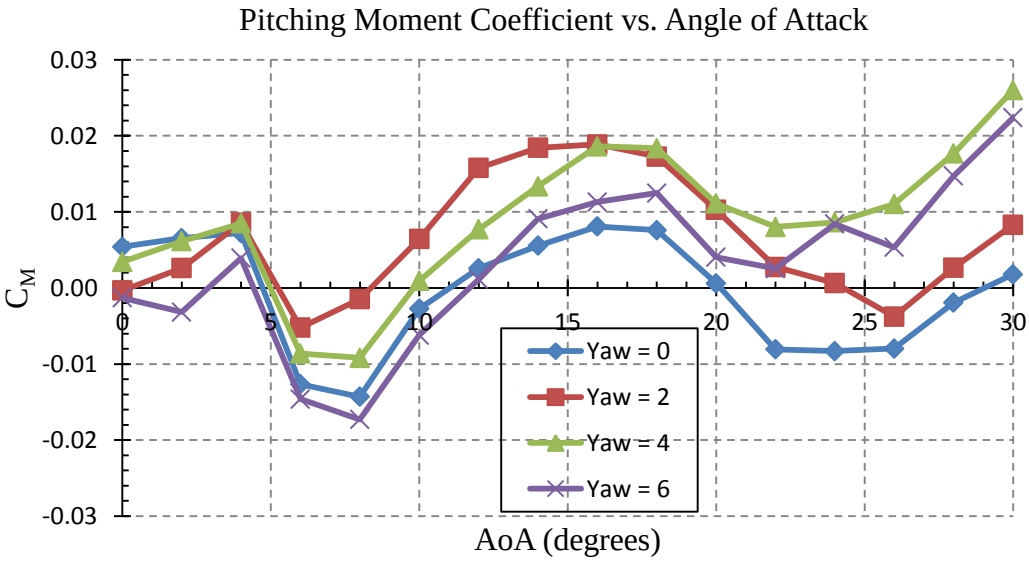

Figure 24. Yaw Angle Effects on Pitching Moment Coefficient, Steady Flow, Re = 2.3 x 10^4.

Side force and yawing moment show similar behavior to pitching moment and are shown in Figure 25.

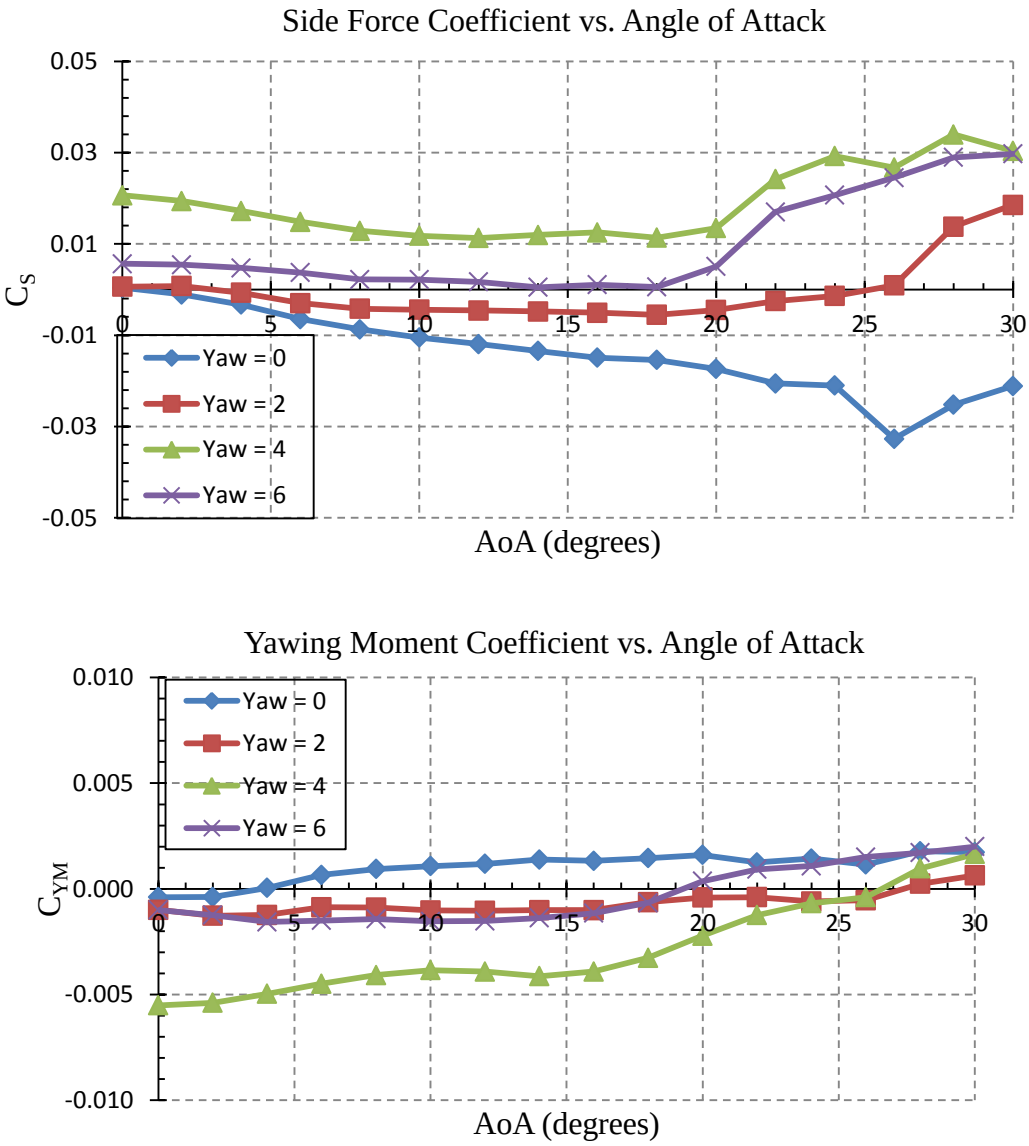

Figure 25. Yaw Angle Effects on Side Force Coefficient (top), and Yawing Moment Coefficient (bottom), Steady Flow, Re = 2.3 x 10^4.

The rolling moment coefficient for the same cases (in Figure 26) shows that the values move from positive to more negative with increasing yaw angle pointing to the role of the asymmetrical vortices.

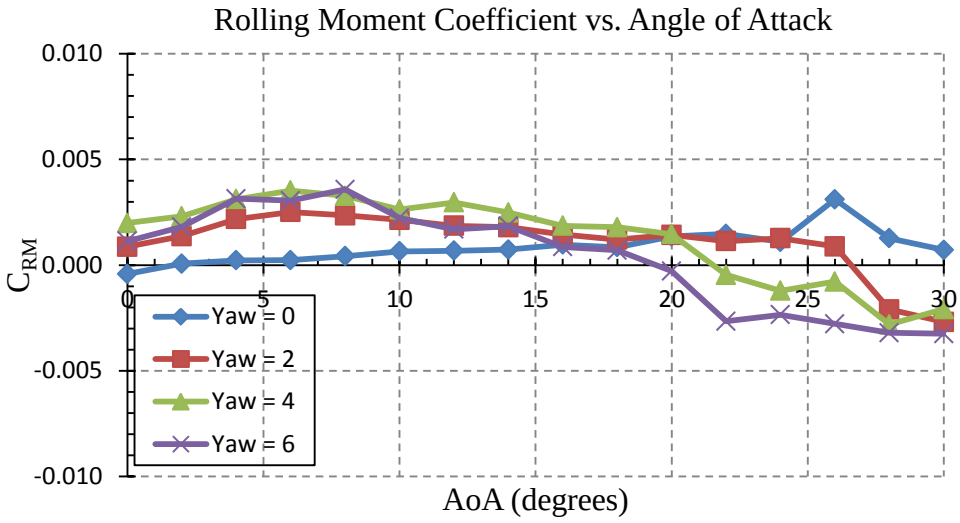

Figure 26. Yaw Angle Effects on Rolling Moment Coefficient, Steady Flow, Re = 2.3 x 10^4.

2. Dynamic Load Measurements

Figure 27 shows the yawed UCAV 1303's performance during the pitch-up maneuver. The normal force distribution trends linearly showing no sign of tip-stall like earlier, as well as having the added benefit of the dynamic lift through 30 degrees. This is the behavior that has been demonstrated of a maneuvering aircraft, and it is beneficial that the yaw does not drastically change this. The yawed aircraft exhibits higher lift forces, which may be exploited as a benefit during maneuver under yawed flights. Yaw does not significantly affect the pitching moment distribution either; C_M trends downward in all cases before ramping up around 12 degrees. In any case, the yawed model demonstrated fewer and less severe pitch-breaks. In the dynamic case, yaw affects the side force coefficient in the opposite way that it did the steady flow cases. In the steady flow case, as yaw was increased, C_S became more positive. In the dynamic case,

C_S becomes more negative. The exact reason for this behavior is unclear, but the side force depends on the formation of asymmetrical vortices, whose preferential behavior to a side is known to be arbitrary. C_{YM} remains near zero.

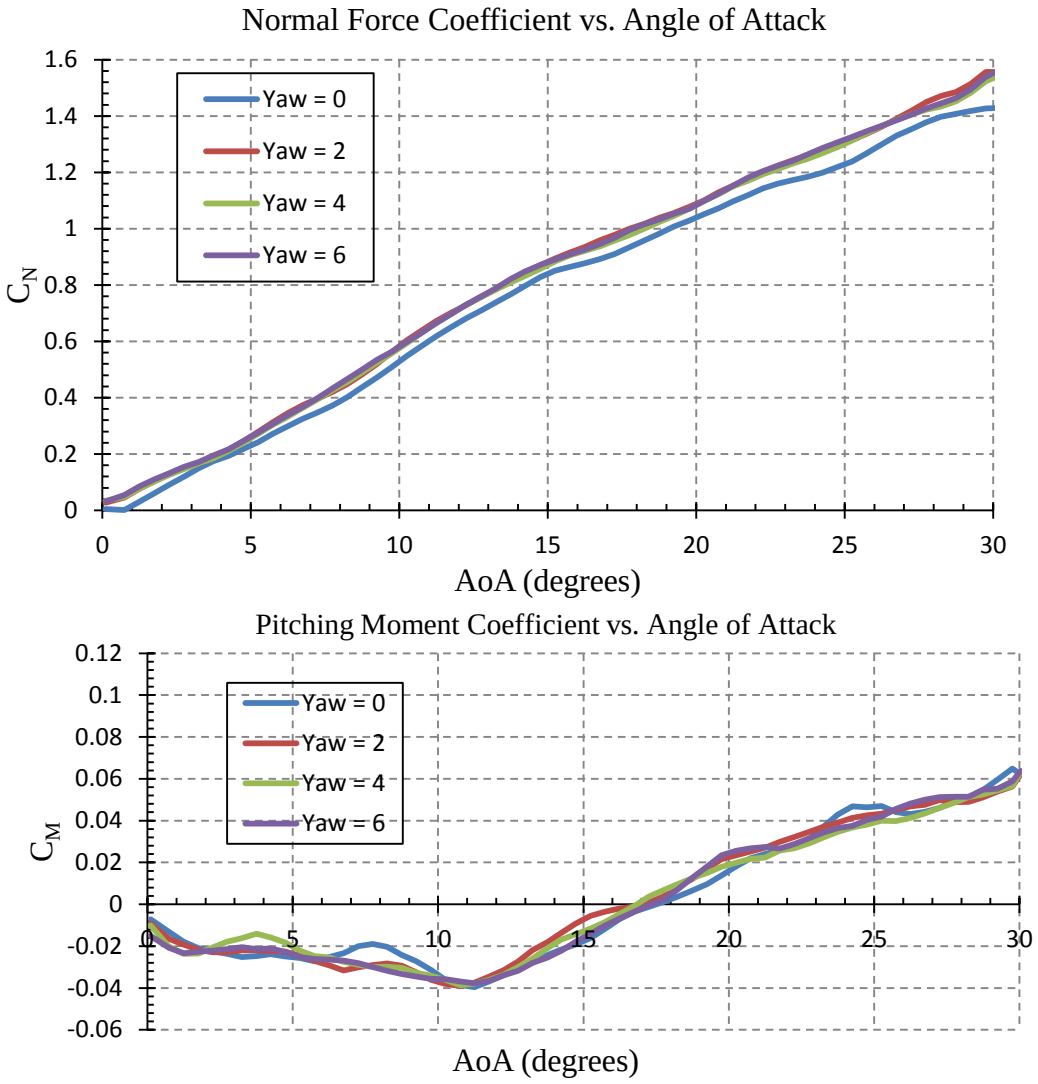

Figure 27. Yaw Angle Effects on (from top to bottom:) C_N, C_M, C_S, C_{YM}, $\alpha+ = 0.05$, Re = 2.3 x 10^4 (continued on next page).

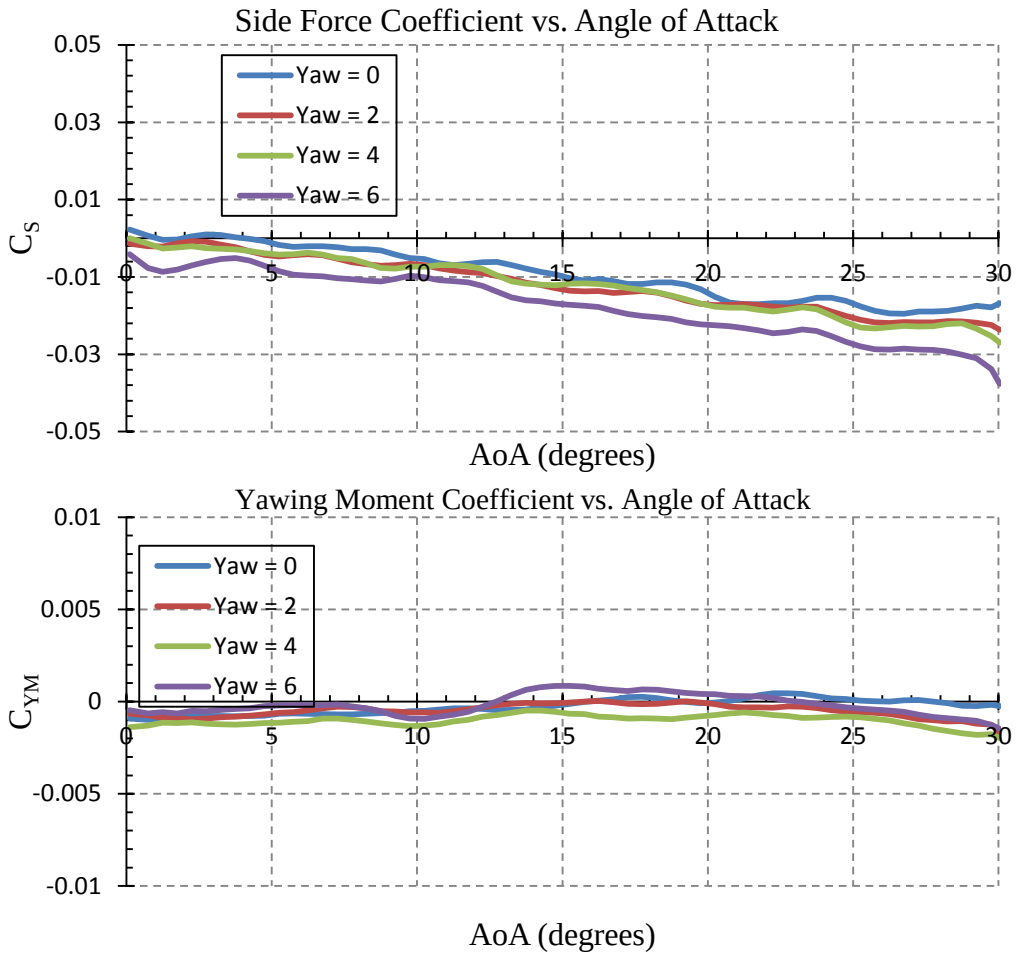

Figure 27. (Continued) Yaw Angle Effects on (from top to bottom:) CN, CM, CS, CYM, $\alpha+ = 0.05$, Re = 2.3 x 104.

The rolling moment coefficient (Figure 28) exhibits the greatest change as a result of a yawed maneuver. At zero incidence, all moments are near zero. As the model pitches through the maneuver, however, the curves separate. The yaw = 0 (blue) curve stays along the zero trend; however, with increasing yaw, the curves dip more negative and later. The dips are also longer with increasing yaw. The yaw = 2 (red), 4 (green), and 6 (purple) curves reach minimums at 11 degrees (-0.001), 11.5 degrees (-0.002), and 12 degrees (-0.004), respectively.

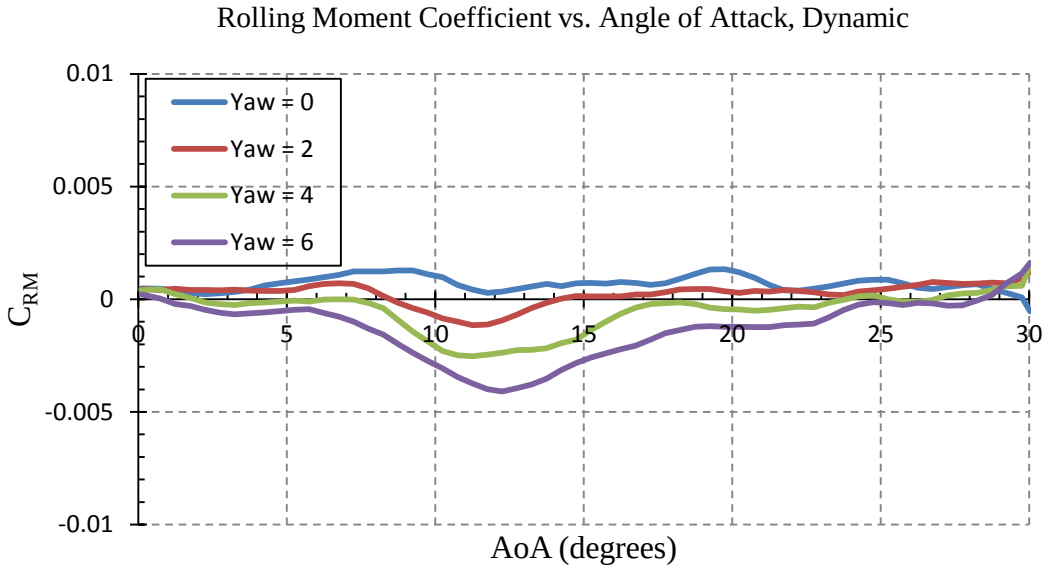

Figure 28. Yaw Angle Effects on Rolling Moment Coefficient, $\alpha+ = 0.05$, Re = 2.3 x 10^4.

E. EFFECT OF LEADING EDGE MODIFICATION

The above experiments were repeated with the modified leading edge. The results in this section will therefore be presented in a twofold manner. First, the effect that the modification had on each measurement will be examined in both the steady and the unsteady flow cases. Then, the effects of Reynolds number, pitch rate, and yaw will be examined. Similar to above, the middle Reynolds number (Re = 2.3 x 10^4) and lower pitch rate ($\alpha+ = 0.05$) will be used for comparisons where neither are the focus variable.

1. Normal Force Distribution

Figure 29 shows the effect that rounding the leading edge has on C_N in steady and unsteady flow. In steady flow, the red, dotted line shows a much more linear trend throughout the lower angles of attack and especially through the angle of attack where tip-stall occurred for the baseline case, demonstrating an alleviated tip-stall. At the higher angles of attack, the modified leading edge (MLE) curve shows a more gradual variation indicating more organized formation. It also attains higher C_N values suggesting that rounding the leading edge causes slightly stronger vortices that have a higher level of

suction at their cores. Although these changes are slight, these were found to be repeatable and were consistent for each run. As can be expected, vortical breakdown occurs which manifests as a loss of C_N, however, this does not imply a total loss of lift since the low pressure region over the wing persists like that seen for the unmodified planform.

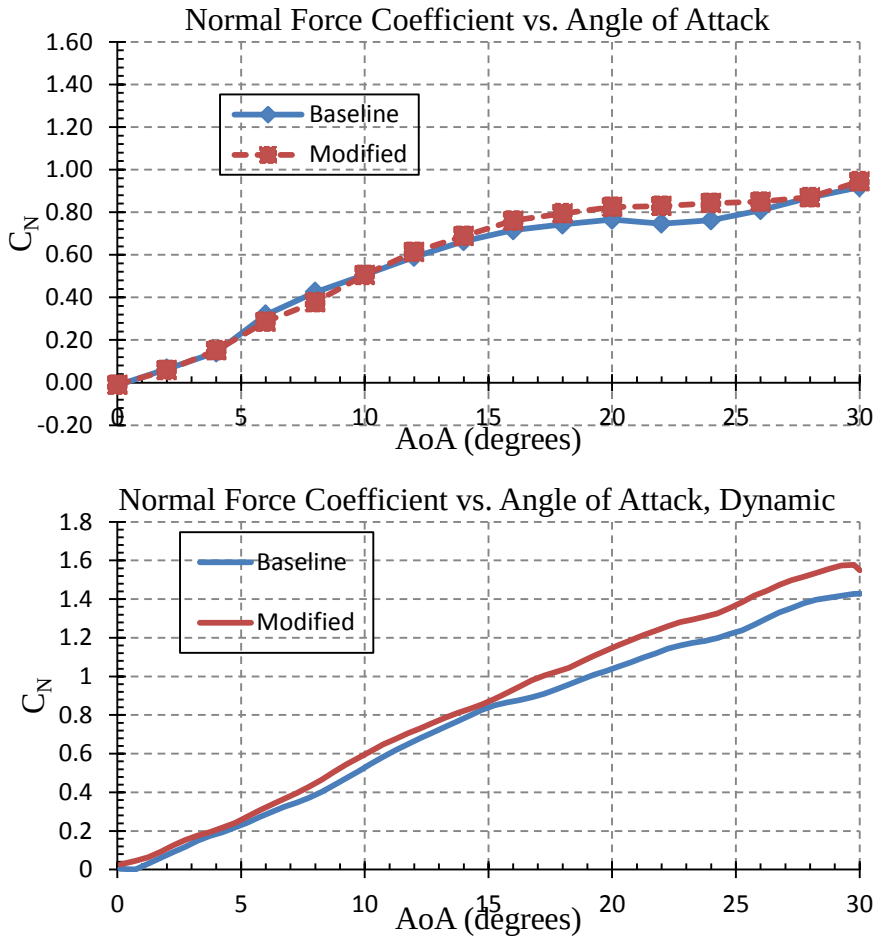

Figure 29. Comparison of Baseline with MLE on C_N, Re = 2.3 x 10^4, Top: $\alpha+ = 0$, Bottom: $\alpha+ = 0.05$.

These results comply with the literature mentioned earlier (although there is no reference to tip-stall alleviation in them) and are an early indication that a more rounded leading edge may be more beneficial.

The Reynolds number effects on the modified model are shown in Figure 30. In all tests, both steady and unsteady, tip-stall is alleviated, and the model shows some response to Reynolds number. In both the steady and unsteady cases, the normal force curves are higher with higher Reynolds numbers. This dependence on Reynolds number appears more distinct relative to the unmodified case studies. The unusual behavior of below zero C_N values between 0 and 2 degree angles of attack was repeated for the case of Re = 1.3 x 10^4 (blue line). It is suspected that at the very low flow rates, the flow is extremely sensitive to even slight geometric irregularities; however, the low Reynolds number case where this effect is observed is also a non-typical flight regime. More investigation into this area should be considered before of a rounder leading is more widely implemented.

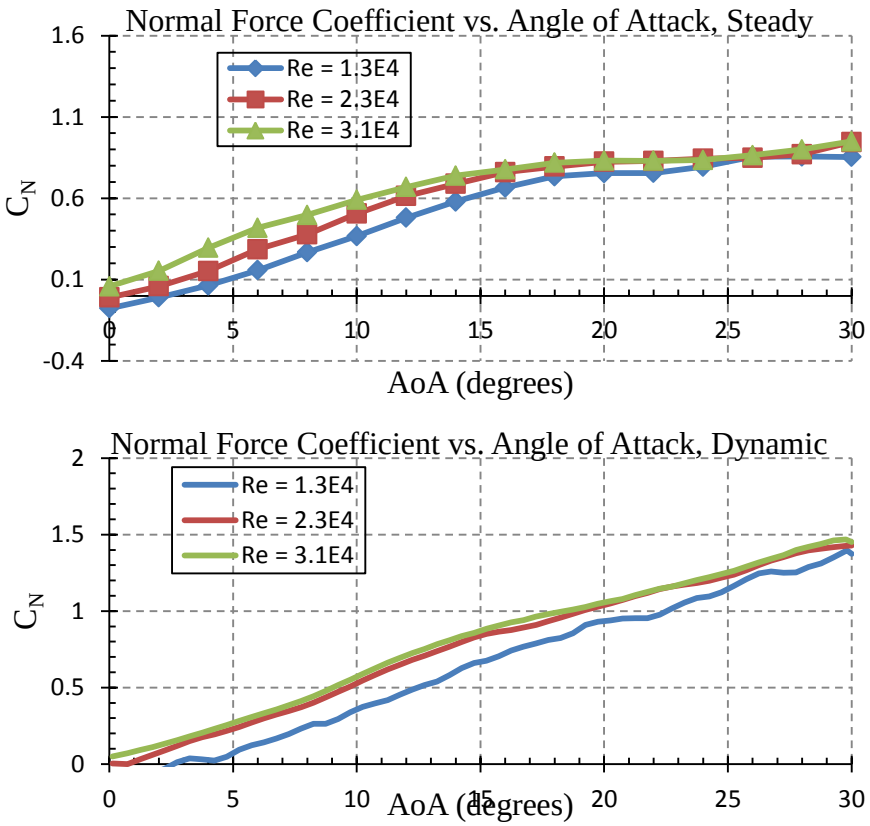

Figure 30. Reynolds Number Effects with MLE on C_N, Top: $\alpha+ = 0$, Bottom: $\alpha+ = 0.05$.

Pitch rate (Figure 31) shows no significant effect at the middle Reynolds number.

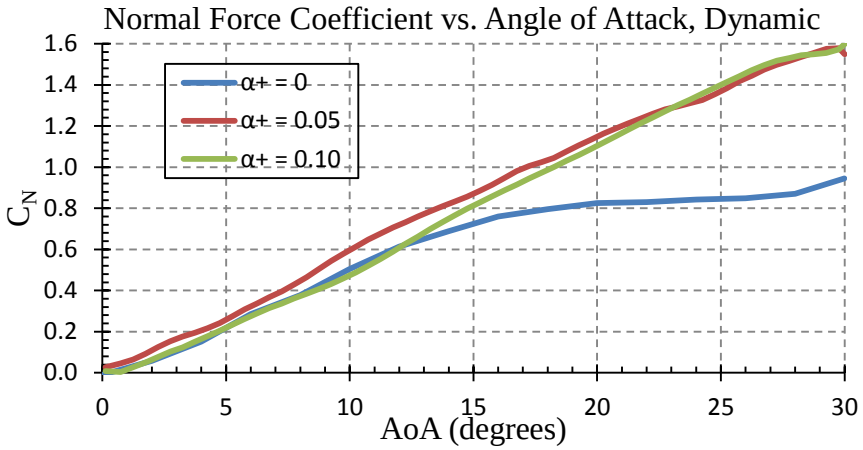

Figure 31. Pitch Rate Effects with MLE on C_N, Re = 2.3 x 10^4.

With a modified leading edge, the yaw effects on C_N are opposite from before. Without the MLE, the lower outlying curve was the yaw = 0 case (Figure 27). With the MLE, the 6 degree yaw case is trending lower than the rest as seen in Figure 32.

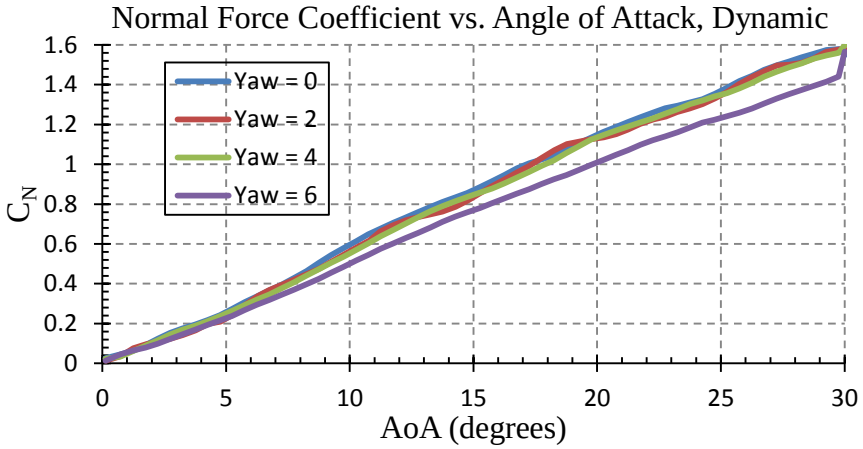

Figure 32. Yaw Angle Effects with MLE on C_N, α+ = 0.05, Re = 2.3 x 10^4.

2. Pitching Moment Distribution

As previously mentioned, one of the problems that tip-stall induces in steady flow is large and sharp pitch-breaks in the C_M plot. This can be seen in the blue, baseline line at 4 degrees in Figure 33. By rounding the leading edge, however, the distributions become noticeably smoother in the tip-stall region of angles of attack. Also, the model has a pitch-down tendency at zero incidence, and does not experience the same pitch-break. The curve seems linear through 5 degrees also. The MLE also creates a more negative C_M until 14 degrees where it crosses the baseline curve. This rise accompanies the extra lifting force shown in the previous section. When the steady curves dip again after 18 degrees as the vortices do slowly break down, the MLE causes a much smoother recovery. In the dynamic case, although tip-stall was not an issue, similar behavior can be seen. The modified model exhibits a lower C_M throughout until about 14 degrees.

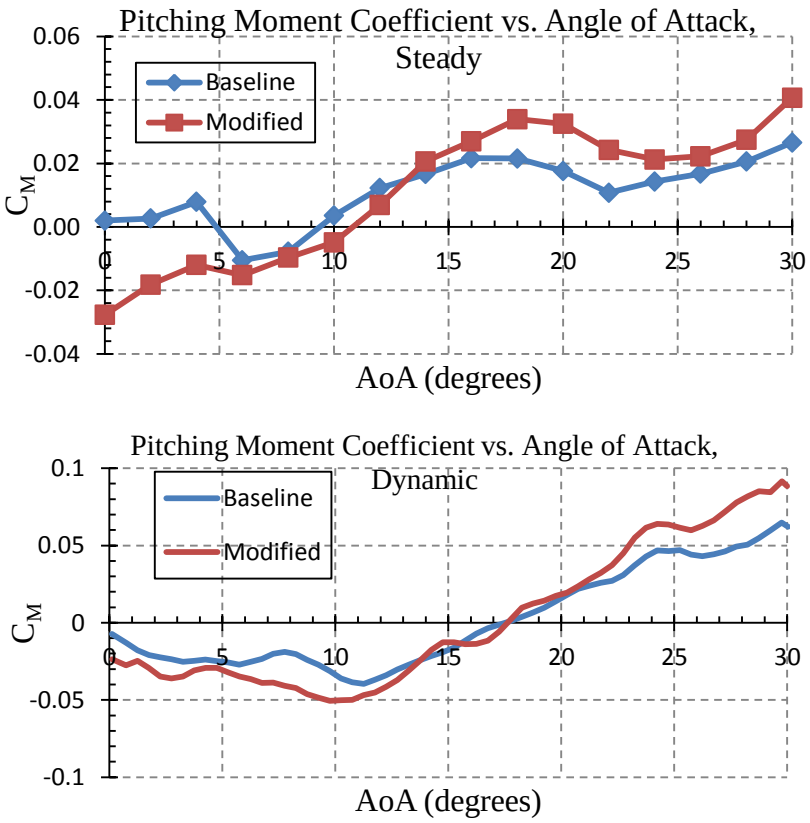

Figure 33. Comparison of Baseline with MLE on C_M, Re = 2.3 x 10^4, Top: $\alpha+ = 0$, Bottom: $\alpha+ = 0.05$.

Reynolds number effects on the C_M behavior of a modified model are shown in Figure 34. At the lowest Reynolds number, the curve is offset to higher values in both steady and unsteady flows. Also, in unsteady flow, the lowest Reynolds number exhibits undue fluctuations. Although the values are low, both these effects should be further investigated. In the static cases, the C_M distributions for the two higher Reynolds numbers are relatively the same; however, for the modified case, slight differences show up in the dynamic case. The highest Reynolds number is generally less negative indicating that rounding the leading edge is actually making the higher Reynolds number case values more suitable. It is suspected that since as Reynolds increases, the viscous effects become diminished, the flow behavior becomes less sensitive to viscous effects that affect the results. These results can only be verified by conducting a systematic study in a wind tunnel, where a larger variation can be created.

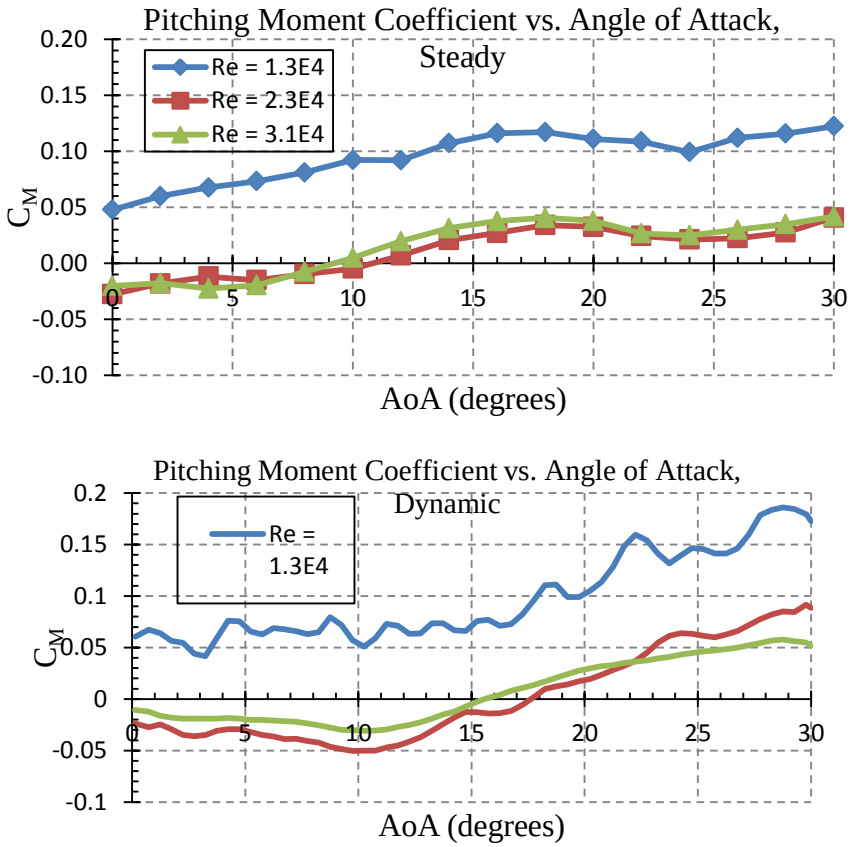

Figure 34. Reynolds Number Effects with MLE on C_M, Top: $\alpha+ = 0$, Bottom: $\alpha+ = 0.05$.

Figure 35 shows that the MLE does not affect the pitch rate effect on C_M. The difference here is that for the lower pitch rate case, C_M starts at a slightly more negative value and stays low until 12 degrees before increasing. The sharper rise seen locally is delayed to about 17 degrees by increasing the pitch rate. It is believed that this effect is similar what is observed in 2-D studies of dynamic stall, where the flow vorticity seems more organized and coherent until higher angles of attack at higher pitch rates. A detailed assessment of dynamic stall research has been conducted by Chandrasekhara and Carr [18].

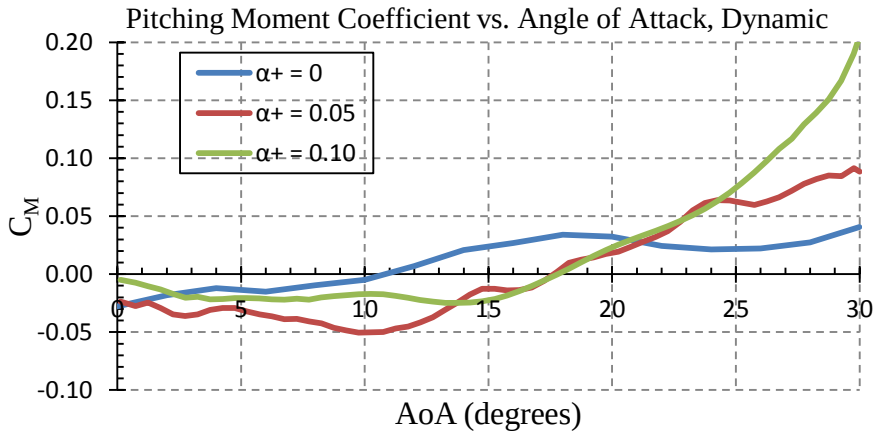

Figure 35. Pitch Rate Effects with MLE on C_M, Re = 2.3 x 10^4.

By modifying the leading edge curvature, the only characteristic changed in yawed pitch-up maneuvers is the values. At the two lower yaw angles, the minimum reached just after 10 degrees is slightly lower. Also, at 30 degrees, the curves ramp to a slightly higher maximum.

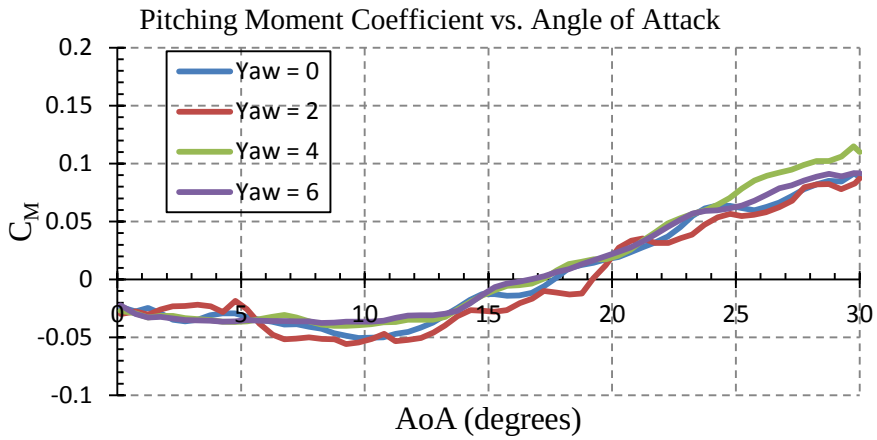

Figure 36. Yaw Angle Effects with MLE on C_M, $\alpha+ = 0.05$, Re = 2.3 x 10^4.

3. Side Force Distribution

In the following section, side force will be examined. Figure 37 shows the effect of increasing the leading edge curvature. In the steady case, it is clear that there is an offset value (with baseline being higher), but the trends are relatively the same. Both curves slope downward which points to a definite asymmetrical vortical flow developing in both cases. The sharper change at 20 degrees is slightly delayed and now occurs at 22 degree for the modified case. Since side forces at zero yaw and high angles of attack are due to asymmetrical vortex formation, one can attribute the difference to the increased leading edge curvature. Similar results are also seen in the dynamic case.

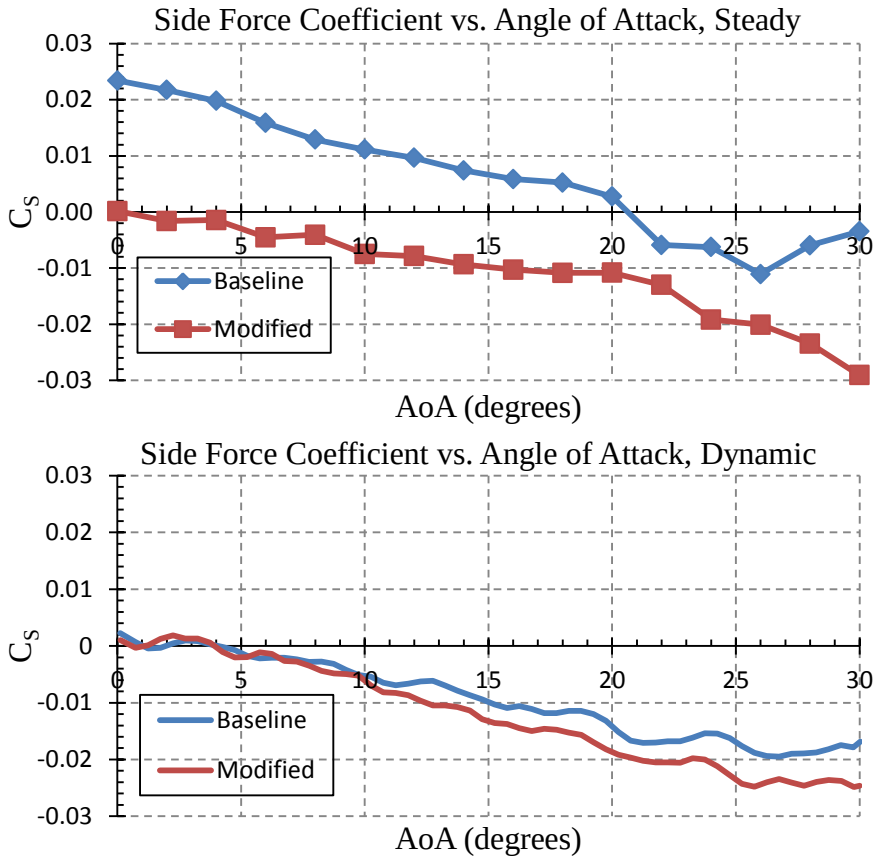

Figure 37. Comparison of Baseline with MLE on C_S, Re = 2.3 x 10^4, Top: $\alpha+ = 0$, Bottom: $\alpha+ = 0.05$.

Reynolds number again shows no consistent effect on side force in either the steady or dynamic case as seen in Figure 38. All MLE curves follow close on top of each other until 24 degrees when the highest Reynolds number tested begins to trend up and down. The lowest Reynolds number pitches up at 26 degrees, whereas the middle Reynolds number continues into the negative direction. Again, these differences may be attributed to asymmetric vortices.

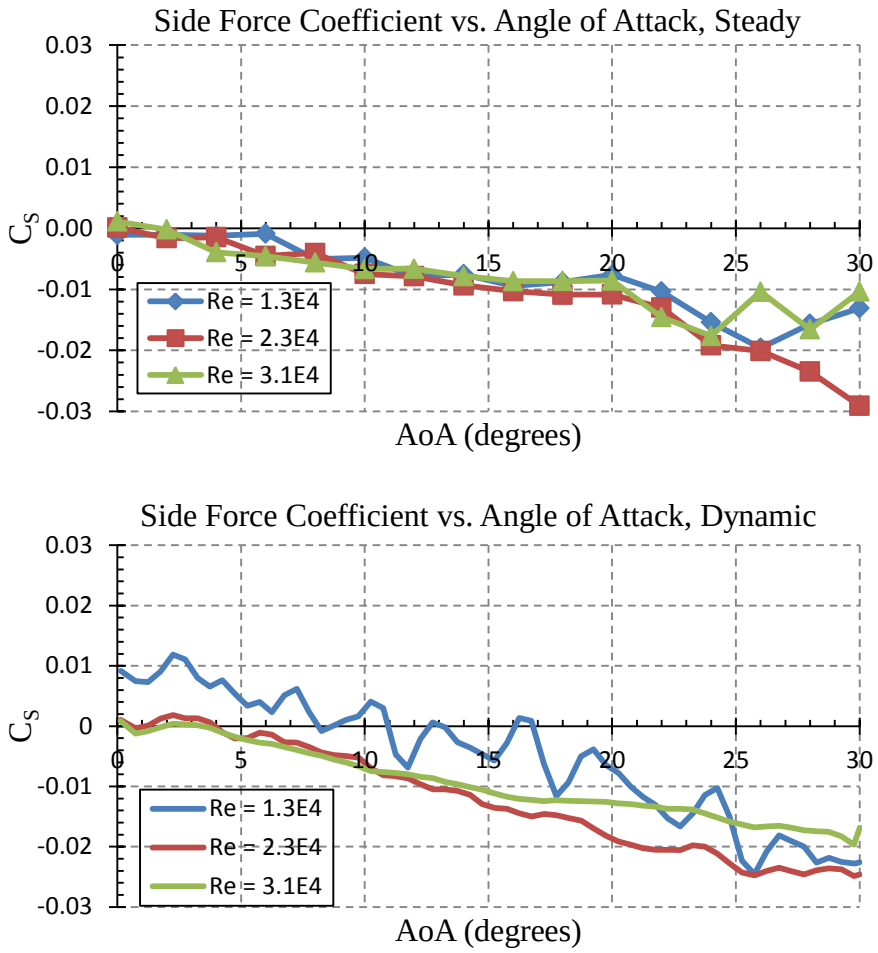

Figure 38. Reynolds Number Effects with MLE on C_S, Top: $\alpha+ = 0$, Bottom: $\alpha+ = 0.05$.

Pitch rate also does not have a particularly dominant effect on side force, as seen in the closely trending curves in Figure 39.

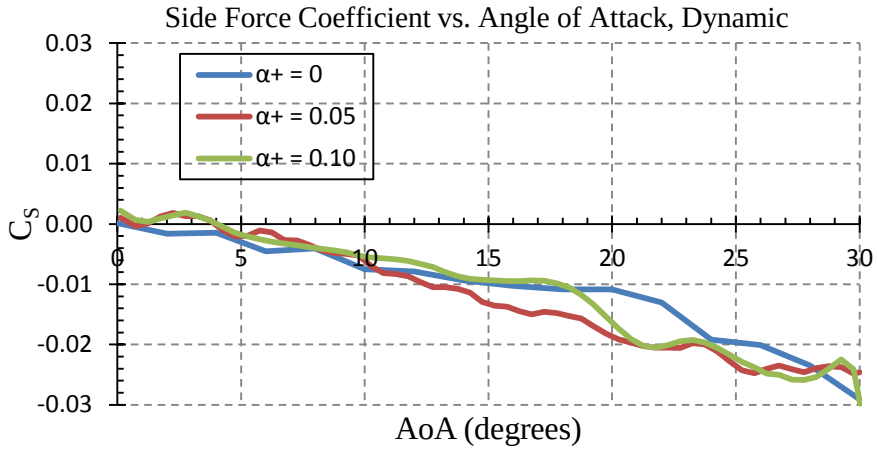

Figure 39. Pitch Rate Effects with MLE on C_S, Re = 2.3 x 10^4.

Yaw effects are shown in Figure 40. All yawed curves (β = 2, 4, and 6 degrees) show similar affects. They all follow the pattern observed for the β = 0 case; however, there are slight bulges in each of the yawed curves at specific angles of attack around 11, 17, 23, and 26 degrees. It is possible that there are new vortical structures that formed due to the increased yaw that introduced similar asymmetries for the non-zero yaw angle cases. Since no flow visualization pictures are available, it is difficult to confirm this inference, but a preferential tendency of the flow observed to swing away from the direction of yaw used at zero degrees lends support to this.

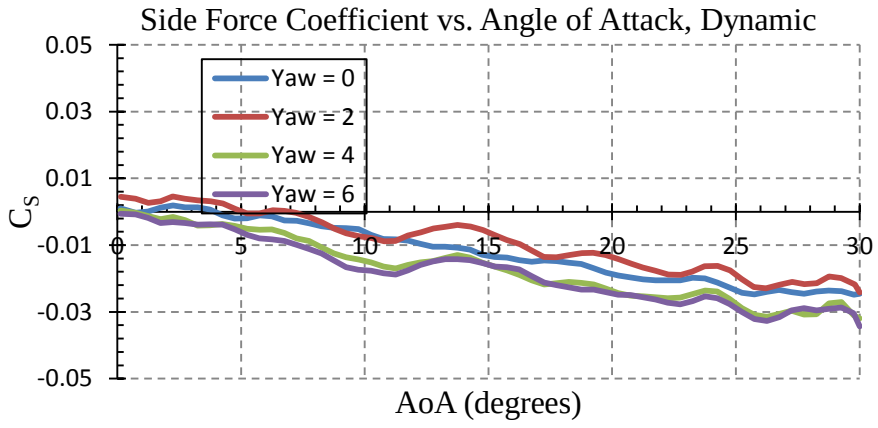

Figure 40. Yaw Angle Effects with MLE on C_S, α+ = 0.05, Re = 2.3 x 10^4.

4. Yawing Moment Distribution

The yawing moment coefficient is a very small quantity; however, for thoroughness it will be included in this discussion. It is important to look at the effects that modifying the airfoil will have on yawing moment since, as previously mentioned, there is no vertical tail or rudder for longitudinal stability. Also, there are currently no reported measurements about the UCAV 1303's yawing moment. Since the UCAV control system has to respond to even subtle changes in these moments, it is expected that the data will provide some new insight into the requirements for this purpose. Figure 41 captures this effect. In the steady case, the trends and values are almost completely opposite. The baseline case begins at -0.008 and trends near-linearly to -0.002. The modified case starts near zero and trends near-linearly to -0.006, maintaining a nearer-to-zero value the entire time until 25 degrees. These opposite slope signs could potentially be once again attributed to asymmetrical vortices since the loads are extremely small. In the dynamic case, yawing moment is negligible.

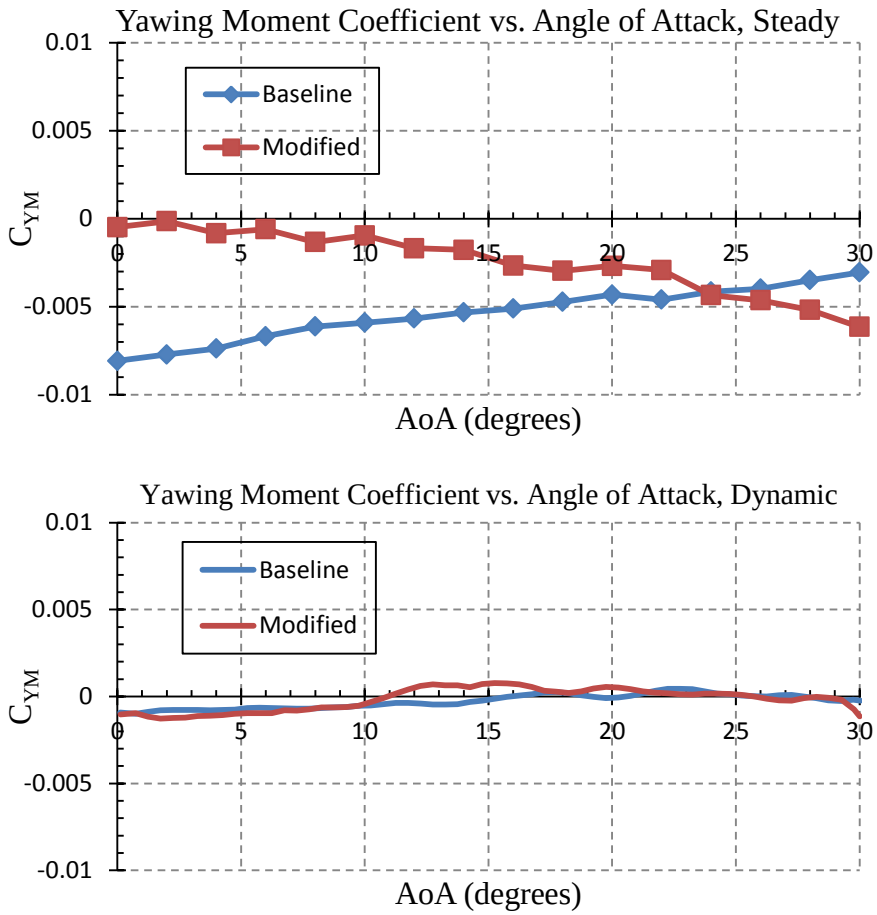

Figure 41. Comparison of Baseline with MLE on C_{YM}, Re = 2.3 x 10^4, Top: $\alpha+ = 0$, Bottom: $\alpha+ = 0.05$.

Figure 42 shows the effect of Reynolds number on C_{YM} for steady and unsteady flows. For the steady case, the lines closely resemble that of the side force coefficient, except the values are significantly smaller. In unsteady flow, the two higher Reynolds numbers again maintain relatively flat curves near zero.

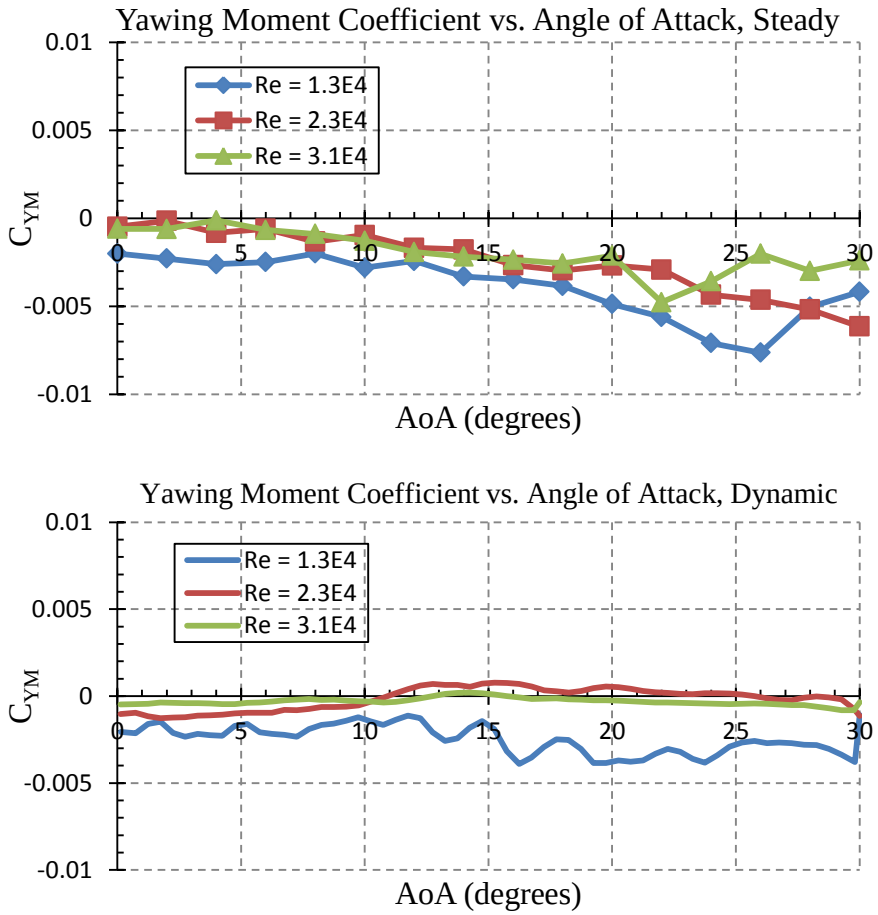

Figure 42. Reynolds Number Effects with MLE on C_{YM}, Top: $\alpha+ = 0$, Bottom: $\alpha+ = 0.05$.

The pitch rate comparison in Figure 43 shows effects not previously seen. All three tests maintain a near zero value of C_{YM} until 10 degrees. At 10 degrees, the steady case ($\alpha+ = 0$) begins to slope negatively down towards -0.006, the second case ($\alpha+ = 0.05$) maintains a near zero value, and the third case ($\alpha+ = 0.10$) also slopes down negatively but only to a final value of -0.004.

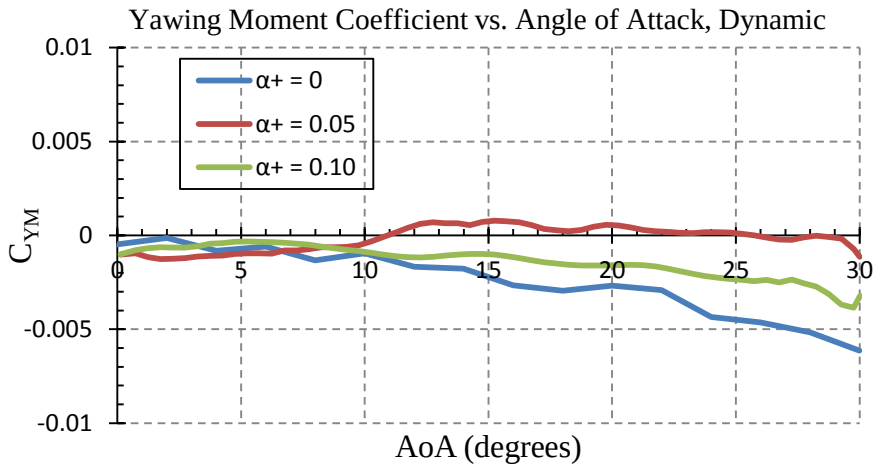

Figure 43. Pitch Rate Effects with MLE on C_{YM}, Re = 2.3 x 10^4.

It is expected that yaw would have the greatest effect on the yawing moment coefficient. At low angles of attack, there is little effect of yaw that was measured. Differences start appearing beyond α = 8 deg, which is around the angle of attack when the vortices start forming. Although the β = 4 degrees and β = 6 degrees cases result in the most negative slopes and values, the final values are still not great enough to warrant special attention. The model is therefore considered suitable with slight crosswind in the yaw direction.

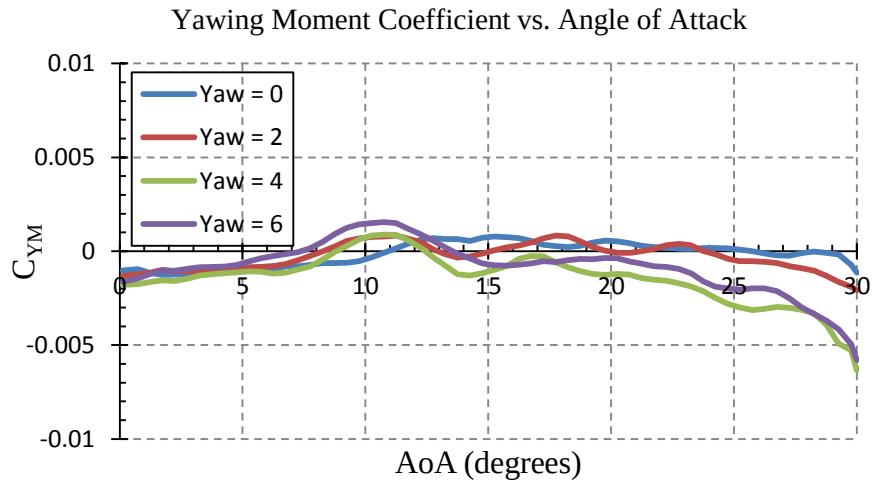

Figure 44. Yaw Angle Effects with MLE on C_{YM}, α+ = 0.05, Re = 2.3 x 10^4.

5. Rolling Moment Distribution

As will be seen, the rolling moment coefficients of the MLE cases show the most difference from baseline. In the NPS load balance, rolling moment is a separately and individually measured quantity (unlike other quantities which are derived from multiple strain gage measurements). Because of the notable differences measured, the measurements were repeated several times and at different speeds, however, the trends seen remained. Hence, they are believed correct and are discussed further. For the baseline model, C_{RM} remains close to zero, with a small change between 20 and 25 degrees. The MLE case rises to an order of magnitude higher, once again attributed to the vortices, but it is suspected that they are asymmetrically spaced on and over the wing to induce such a large change. In the dynamic case, this large growth in rolling moment is no longer present (but only in the higher Reynolds numbers as will be seen). The baseline case remains near zero, and with the exception of a local rise between 11 and 14 degrees, the MLE case does as well.

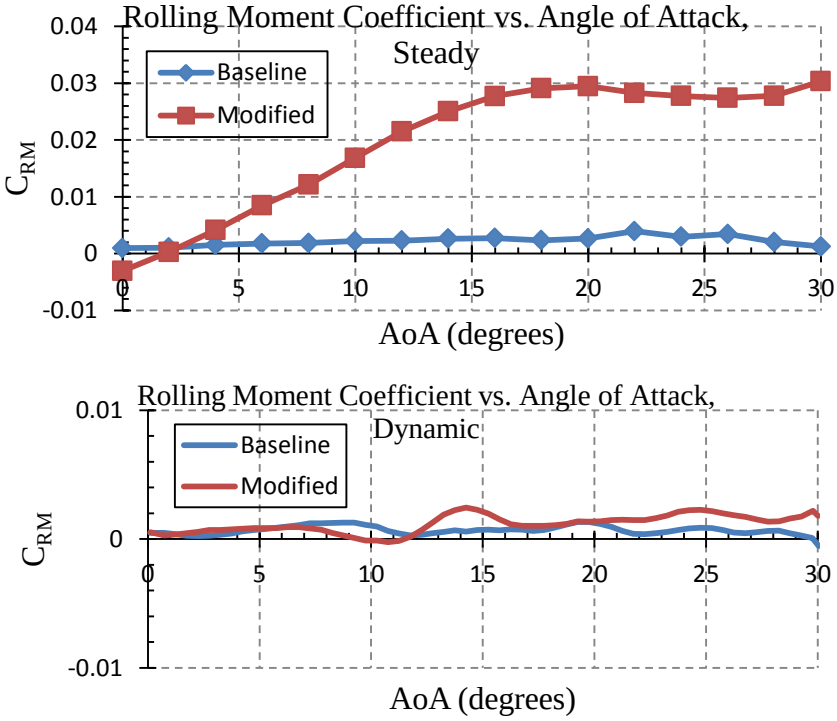

Figure 45. Comparison of Baseline with MLE on C_{RM}, Re = 2.3 x 10^4, Top: $\alpha+ = 0$, Bottom: $\alpha+ = 0.05$.

Figure 46 shows the MLE's effect on the rolling moment's sensitivity to Reynolds number. A growth of values is seen in all three steady cases as a result of the strong vortices. The lowest Reynolds number has the highest C_{RM} values, while the middle number has the lowest C_{RM} values. The highest Reynolds number remains in between these values, closely matching Re = 1.3 x 10^4's curve until halfway at 15 degrees where it drops slightly and then closely matches Re = 2.3 x 10^4's curve. In the dynamic case, the lowest Reynolds number shows linear growth to 0.05. The rolling moment at 30 degrees of this case is almost double the rolling moments produced during steady flow. The higher Reynolds number values remain close to zero.

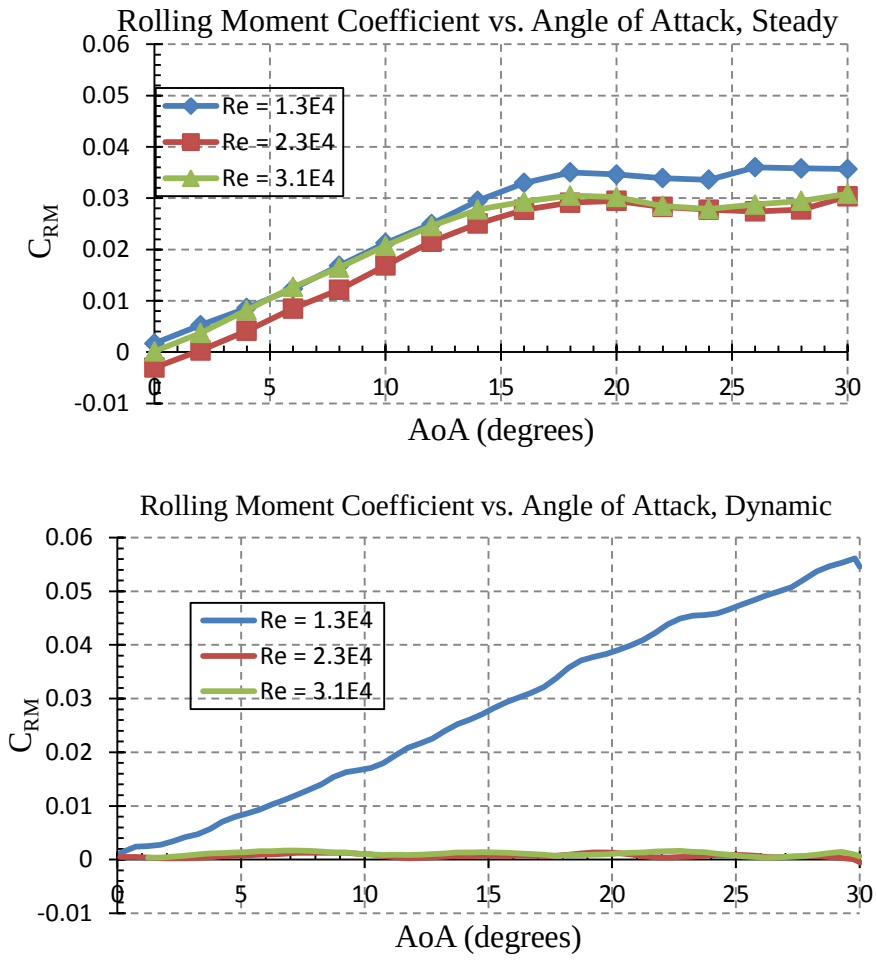

Figure 46. Reynolds Number Effects with MLE on C_{RM}, Top: $\alpha+ = 0$, Bottom: $\alpha+ = 0.05$.

Figure 47, the effect of pitch rate on rolling moment, presents interesting data that has been repeated in water tunnel experiments. For $\alpha+ = 0.10$, the highest pitch rate examined, the trend follows the same linear growth pattern of the lower Reynolds number dynamic runs. For $\alpha+ = 0.05$, the trend is near zero, matching the higher Reynolds number cases. The only rise in value is at higher angles of attack, which once again can be attributed to the asymmetrical vortical flow over the wings.

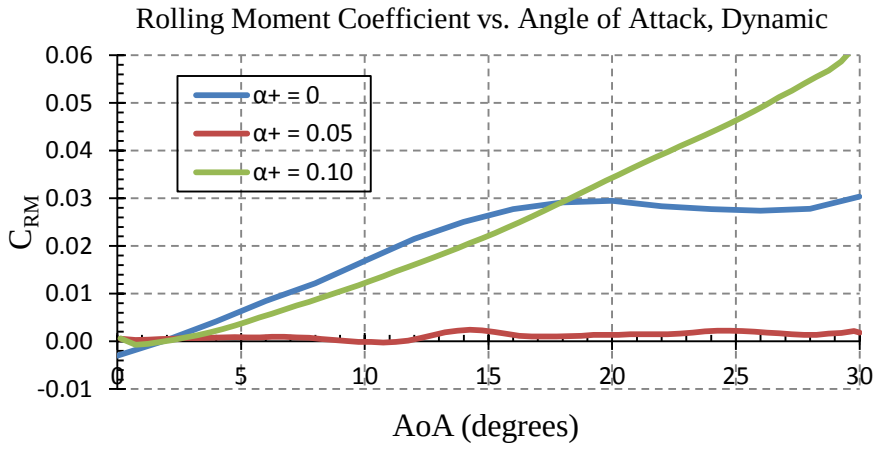

Figure 47. Pitch Rate Effects with MLE on C_{RM}, Re = 2.3 x 10^4.

The nonzero yaw angles in Figure 48—which shows the effects of yaw on a pitch-up maneuver—all exhibit the previously displayed linear growth. The greatest value is $\beta = 2$, which is higher than $\beta = 4$, which is in turn higher than $\beta = 6$.

If this data is correct, than the rolling moment would be the most significant effect for which a control system would have to account if the leading edge is rounded as in the present experiments.

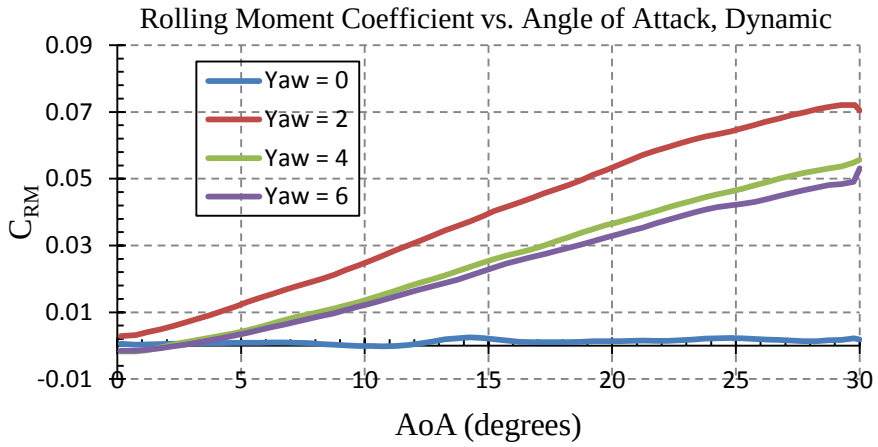

Figure 48. Yaw Angle Effects with MLE on C_{RM}, $\alpha+ = 0.05$, Re = 2.3 x 10^4.

IV. CONCLUDING REMARKS

The present experiments provided some qualitative and detailed quantitative results of a baseline as well as modified UCAV 1303. Recorded baseline flow visualization and load data measurements have been shown to validate this experiment with previously attained data. The flow sensitivity to leading edge curvature also was exploited to create the modified UCAV 1303 flow. The modified model examined the effect of modifying the leading edge curvature on the aerodynamic coefficients of the tailless vehicle. This second component of the study was performed in an attempt to control undesirable flow features such as tip-stall and pitch-breaks observed in the original baseline model flow. Additionally, the experiments inspected the effect on load measurements with regards to a rounded leading edge's sensitivity to Reynolds number, pitch rate, and constant yaw and are some of the first of their kind to include maneuvering load experiments.

Preliminary results showed positive feedback regarding the doubling of the model's leading edge radius. Tip-stall has been alleviated in the normal force distributions, and the associated pitch-breaks have also been smoothened. The design is also relatively unaffected by Reynolds number and reacts better to a more rapid maneuver. One observed drawback is that the rise of pitching moment occurred at a slightly lower angle of attack in the modified case. The model also showed resistance to a yawed position—used to simulate crosswind—during maneuver. A steady pitch-up motion has also been proven to alleviate tip-stall as well as double the lift at an incidence of 30 degrees; however, in steady flight, curvature change seems to be necessary for tip-stall mitigation. The rolling moment has been shown to rise as incidence increases and will require further investigation.

In order to mitigate and discover the cause of some of the disadvantages, such as the rolling moment, flow visualization will need to be performed with the rounded leading edge. Tests examining different size leading edge radii should also be conducted,

as well as tests wherein the leading edge curvature is modified only locally. The latter sectional change idea may prove to be better, if its rolling moment characteristics can be favorably influenced.

LIST OF REFERENCES

[1] M. S. Chandrasekhara and B. K. McLain, "Aerodynamic studies over a maneuvering UCAV 1303 configuration," *Aeronautical Journal*, Accepted for Publication.

[2] G. M. Billman and B. A. Osbourne, "High L/D extended range/payload fighter aircraft technology," *AFRL-VA-WP-TR-1999–3084*, November 1998.

[3] B. K. McLain, "Steady and unsteady aerodynamic flow studies over a 1303 UCAV configuration," M.S. thesis, Naval Postgraduate School, 2009.

[4] I. Gursul, R. Gordnier and M. Visbal, "Unsteady aerodynamics of nonslender delta wings," *Progress in Aerospace Sciences*, vol. 41, pp. 515–557, 2005.

[5] H. Werle, "Sur l'eclatement des tourbillons," *ONERA, Note Technique*, no. 175, November 1971.

[6] A. S. Bova, G. L. Lang, G. L. Blaisdell, J. Gibson and T. Niessen, "Investigation of vortex bursting at a low reynolds number," *International Journal of Fluid Dynamics*, vol. 5, pp. 31–40, 2001.

[7] D. W. Moore and D. I. Pullin, "Inviscid separated flow over a non-slender delta wing," *Journal of Fluid Mechanics*, vol. 305, pp. 307–345, 1995.

[8] G. S. Taylor, T. Schnorbus and I. Gursul, "An investigation of vortex flows over low sweep delta wings," in *AIAA Fluid Dynamics Conference and Exhibit*, Orlando, Florida, 23–26 June 2003.

[9] S. C. McParlin, R. J. Bruce, A. G. Hepworth and A. J. Rae, "Low speed wind tunnel tests on the 1303 UCAV concept," *AIAA-2006–2985*, 2006.

[10] K. Petterson, "CFD analysis of the low-speed aerodynamics characterstics of a UCAV," *AIAA-2006–1259*, 2006.

[11] D. W. Wong, G. J. McKenzie, M. V. Ol, K. Petterson and S. Zhang, "Joint TTCP CFD studies into the 1303 UCAV performance," *AIAA-2006–2984*, 2006.

[12] P. D. Sosebee, "Flow visualization and detailed load measurements over a maneuvering UCAV 1303," M.S. thesis, Naval Postgraduate School, 2011.

[13] M. V. Ol, "Water tunnel velocimetry results for the 1303 UCAV configuration," *AIAA-2006–2990*, 2006.

[14] R. M. Cummings, S. A. Morton and S. G. Siegel, "Numerical prediction and wind tunnel experiment for a pitching unmanned combat air vehicle," *Aerospace Science and Technology Journal*, vol. 12, pp. 355–364, December 2008.

[15] J. J. Miau, K. T. Kuo, W. H. Liu, S. J. Hsieh, J. H. Chou and C. K. Lin, "Flow developments above 50-deg sweep delta wings with different leading-edge profiles," *J.Aircr*, vol. 32, no. 4, pp. 787–794, 1995.

[16] H. Kawazoe, Y. Nakamura, T. Ono and Y. Ushimaru, "Static and total pressure distributions around a thick delta wing with rounded leading-edge," *AIAA-94–2321*, 1994.

[17] M. Kerho and B. R. Kramer, *Research water tunnels,* El Segundo, CA, Rolling Hills Research Corporation, 2003.

[18] L. W. Carr and M. S. Chandrasekhara, "Compressibility effects on dynamic stall," *Prof. Aerospace Sci.,* vol. 32, pp. 523–573, 1996.

INITIAL DISTRIBUTION LIST

1. Defense Technical Information Center
   Ft. Belvoir, Virginia

2. Dudley Knox Library
   Naval Postgraduate School
   Monterey, California

3. Professor M.S. Chandrasekhara
   Department of Mechanical and Astronautical Engineering
   Room Wa-320
   Naval Postgraduate School
   Monterey, California

4. Professor G. V. Hobson
   Department of Mechanical and Astronautical Engineering
   Naval Postgraduate School
   Monterey, California

5. Professor K. T. Millsaps
   Department of Mechanical and Astronautical Engineering
   Naval Postgraduate School
   Monterey, California

6. Professor Yeo Tat Soon, Director
   Temasek Defence Systems Institute
   National University of Singapore

7. Mr. Leo Tin Boon, Senior Associate Director
   Temasek Defence Systems Institute
   National University of Singapore

8. Ms. Stephanie Teo
   Temasek Defence Systems Institute
   National University of Singapore